

1 **From long- to short-term inter-plate coupling at the subducted Carnegie Ridge crest,**
2 **offshore Central Ecuador**

3
4 J-Y Collot¹, J-N. Proust², J-M Nocquet¹, C. Martillo³, F. Michaud^{1,4}, J-F. Lebrun⁵, L.
5 Schenini¹, S. Popescu⁶, M-J. Hernandez⁷ and G. Ratzov¹.

6
7
8 ¹ Université Côte d'Azur, IRD, CNRS, Observatoire de la Côte d'Azur, Geoazur, F06560
9 Valbonne, France.

² Université de Rennes, CNRS, Géosciences-Rennes, F-35000 Rennes, France.

11 ³ Escuela Superior Politécnica del Litoral, GEMAC-FIMCM-CADS, P.O. Box 09-01-5863,
12 Guayaquil, Ecuador

13 ⁴ Sorbonne Université, Institut des Sciences de la Terre, 75252, PARIS cedex 05, France

14 ⁵ Geosciences Montpellier, Université des Antilles, Université de Montpellier, CNRS,
15 Pointe à Pitre, Guadeloupe (FWI)

16 ⁶ Geobiostratdata.Consulting, 69140, Rillieux la Pape, France

17 ⁷ Escuela Politécnica Nacional, Departamento de Geológica, Ladrón de Guevara E11-253,
18 Quito, Ecuador

19
20
21
22 Corresponding author: Jean-Yves Collot (jean-yves.collot@ird.fr)

23
24
25
26
27 **Key Points:**

28 - A trench-parallel strike-slip fault and its earthquake-controlled fault scarps substantiate a
29 pre-1.8 Ma, outer-wedge inter-plate coupling

30 - From 1.8 Ma, a robust shelf uplift caused by subducted reliefs highlights a long-term
31 coupling that led to geodetically locked patches

32 - The shallowest subducted relief likely impeded the generation of a major tsunami during
33 the Mw7.8, 2016 event
34

Abstract:

We investigate the relationship between the long-term (Quaternary) interplate coupling and the short-term geodetically derived interseismic coupling at the Central Ecuador subduction zone. At this nonaccretionary margin, the Cabo Pasado shelf promontory and coastal area are associated with two inter-plate geodetically locked patches. The deepest patch ruptured coseismically during the Mw7.8-2016 Pedernales earthquake, while the shallowest underwent dominantly after-slip. Marine geophysical and chronostratigraphic data allow reconstructing the Quaternary tectonic evolution of the shelf promontory and substantiating variation of the long-term inter-plate coupling that led to the geodetically locked patches. Prior to ~1.8 Ma, the outer-wedge inter-plate coupling was strong enough to activate trench-subparallel strike-slip faults. Then, between ~1.8-0.79 Ma, shortening and uplift affected the shelf promontory, implying a locally increased inter-plate coupling. After a short, post-0.79 Ma period of subsidence, shortening and uplift resumed denoting a high inter-plate coupling that endured up to the present. The synchronicity of the structural evolution of the shelf promontory with the subduction chronology of two reliefs of the Carnegie Ridge crest suggests that the locked patches are caused by a geometrical resistance to subduction that propagates landward causing permanent deformation. In 2016, the deepest subducted relief localized stress accumulation and high seismic slip, while the shallowest relief, which is associated with a weakened outer-wedge, prevented updip rupture propagation. Thus, at nonaccretionary margins, active outer-wedge strike-slip faults might be considered a proxy of near-trench coupling, and subducted relief a cause of plate coupling but an obstacle to the tsunami genesis when the relief is shallow.

Plain Language Summary

The 2016-Ecuador earthquake ruptured a subduction fault segment previously locked for decades beneath the coastline. The rupture was arrested updip by another locked fault segment called locked patch, which instead slipped slowly. To understand the cause of the locked patches, their rupture behaviors, and whether the decadal fault locking and long-term subduction processes are related, we reconstructed the Quaternary tectonic evolution of the margin offshore Central Ecuador using geophysical data. We consider that tectonic deformation reflects the long-term inter-plate coupling, which is the ability of the fault to transfer long-term stress and strain to the margin. Prior to ~1.8 Ma, a trench-subparallel fault accommodating lateral displacement indicates a shallow plate coupling, which increased locally between ~1.8-0.79 Ma as shown by margin shortening. After a brief subsidence, shortening resumed, denoting a strong coupling that persisted until today in the form of the locked patches. Although many physical factors have been proposed to control plate coupling, here we find that the locked

69 patches are caused by the subduction of two reliefs of a submarine ridge. Remarkably, in 2016,
70 the deepest relief released high elastic strain, while the shallower relief, thrust under a weakened
71 outer-margin, damped updip rupture propagation, impeding a significant tsunami.

72 **1. Introduction:**

73 In subduction zones, Global Positioning System (GPS) data have been used to demonstrate
74 inter-seismic locked patches to correlate well with regions of high co-seismic slip ([Bilek and](#)
75 [Lay, 2018](#)). Although major earthquakes may alter the inter-plate coupling over a decadal-scale
76 ([Philibosian et al., 2014](#)), in many locations, subduction earthquakes have repeatedly ruptured
77 the same fault segment as exemplified in Ecuador over the past 110 yr ([Ye et al., 2016](#); [Nocquet](#)
78 [et al., 2017](#)), in central Peru ([Perfettini et al., 2010](#)) and southern Chile ([Moreno et al., 2010](#))
79 over several centuries. These observations point to some persistence of the megathrust
80 properties through several earthquake cycles. Paleo-seismology provides evidence of a ~10 ka
81 persistence of the plate coupling and barriers to megathrust rupture propagation ([Goldfinger et](#)
82 [al., 2012](#)).

83 On the scale of the earthquake cycle, simple models only consider elastic rheology where
84 inter-seismic and co-seismic stress/strain would cancel over several cycles. At longer time
85 scales (>100 ka), irreversible anelastic deformation also occurs within the fore-arc and
86 cumulates through time ([Matsuura and Sato, 1989](#)). Possible mechanisms are one or a
87 combination of (1) subduction earthquakes and subsequent post-seismic deformation not
88 relieving all of the strain accumulated during inter-seismic period, (2) plastic deformation
89 occurring as inter-seismic stress exceeds the yield stress, (3) damages occurring close to the
90 plate interface as well as fore-arc folding and faulting. The fraction of the documented short-
91 term strain converting to permanent deformation remains poorly known, with estimates ranging
92 from less than 4% to ~10% ([Allmendinger et al., 2005](#); [Baker et al., 2013](#); [van Dinther et al.,](#)
93 [2013](#); [Jolivet et al., 2020](#)). However, regardless of the magnitude of this ratio, several studies
94 highlight the similarity between the spatial pattern of the inter-seismic strain and that of the
95 permanent deformation ([Allmendinger et al., 2005](#); [Béjar-Pizarro et al., 2013](#); [Jolivet et al.,](#)
96 [2020](#)).

97 Beyond the GPS-derived inter-plate coupling that expresses the fault kinematic during the
98 earthquake cycle ([Wang and Dixon, 2004](#)), the Coulomb wedge theory ([Davis et al., 1983](#);
99 [Lallemant et al., 1994](#); [Wang and Hu, 2006](#)) indicates that the average state of convergent
100 margin deformation over a long-time period depends, amongst other parameters, on the long-
101 term basal friction, and varies from compressively critical to extensionally critical. Therefore,

102 reconstructing the detailed, $\sim 10^5$ - 10^6 -years' time-scale, structural evolution of the margin
103 wedge can inversely provide information on the inter-plate strength that characterizes the long-
104 term plate coupling (e.g., [Victor et al. \(2011\)](#); [Saillard et al. \(2017\)](#)). Following this rationale,
105 scrutinizing the activity of fore-arc faults that root in the megathrust can substantiate the long-
106 term behavior of plate coupling. Mechanical models show that splay faults can transfer slip to
107 the seafloor during megathrust events ([Kame et al., 2003](#); [Wang and Hu, 2006](#)). Indeed, splay
108 faults have been shown to slip co-seismically in Nankai ([Yamaguchi et al., 2011](#)) and Chili
109 ([Lieser et al., 2014](#)), and such repeated activity has been inferred in the Arauco bay in Chili
110 (Jara-Muñoz et al., 2017), and Alaska, where Liberty et al. (2019) suggest a millennial-scale
111 persistence of the 1964 earthquake asperity. Similarly, ten Brink and Lin (2004) show that
112 seismic slip on the megathrust plays a significant role in the slip of upper-plate strike-slip faults,
113 contributing to long-term strain partitioning ([Fitch, 1972](#)).

114 This study combines marine geophysical data, and sedimentary cores collected offshore
115 Central Ecuador (Fig. 1) to decipher the Quaternary activity of a strike-slip fault system that
116 roots in the megathrust (Fig. 2) and extends across an inter-seismic locked patch (the Cabo
117 Pasado (CP) patch), and a creeping barrier ([Chlieh et al., 2014](#); [Nocquet et al., 2017](#)) (Fig. 1b,
118 c). Based on the lifespan of the strike-slip fault system and the subsequent detailed structural
119 evolution of the margin wedge, we (i) estimate the Quaternary variation of the shallow
120 megathrust coupling, (ii) investigate its cause and relationship to geodetic inter-seismic
121 coupling (ISC), as well as the reasons for the spatial distribution of seismic and aseismic slip,
122 and (iii) discuss the styles of permanent deformation associated with a change in megathrust
123 slip mode from stick and slip ([Scholz, 1998](#)) to transient aseismic slip ([Schwartz and Rokosky,](#)
124 [2007](#)).

125 2. Geodynamic setting, seismicity, and inter-seismic coupling

126 In absence of a frontal accretionary wedge ([von Huene and Scholl, 1991](#)), the convergent
127 margin of Ecuador is considered nonaccretionary and controlled by basal erosion ([Sage et al.,](#)
128 [2006](#)). It is underthrust eastward by the Carnegie Ridge (CR), a 14-19 km-thick and buoyant
129 oceanic feature ([Lonsdale, 1978](#); [Graindorge et al., 2004](#); [Sallares et al., 2005](#)) carried along by
130 the Nazca plate at 4.7 cm/yr with respect to the North Andean sliver ([Nocquet et al., 2014](#)) (Fig.
131 1a). Land-based GPS and seismological measurements have revealed that North of Cabo
132 Pasado (Fig. 1b), the plate interface shows strong ISC ([Chlieh et al., 2014](#); [Nocquet et al., 2014](#);
133 [Gombert et al., 2018](#)) and has produced a remarkable seismic sequence that started with the
134 great Mw 8.6-8.8, 1906 earthquake ([Kelleher, 1972](#); [Kanamori and McNally, 1982](#); [Ye et al.,](#)

135 [2016](#)). Four Mw 7.7 to 8.2 earthquakes ([Beck and Ruff, 1984](#); [Mendoza and Dewey, 1984](#);
136 [Swenson and Beck, 1996](#)), including the Mw 7.8, 2016 Pedernales earthquake, later broke sub-
137 segments of the same area (Fig. 1a). In contrast, south of Cabo Pasado, no events with Mw >
138 7.0-7.2 have ruptured the plate interface, and the megathrust shows low ISC ([Chlieh et al., 2014](#);
139 [Nocquet et al., 2014](#)), forming a creeping barrier ([Gombert et al., 2018](#)) that has remained
140 persistent over the last earthquake cycles (Fig. 1b). This remarkable segmentation in
141 seismogenic behavior and ISC along strike the Ecuador margin is likely related to variations in
142 structure and composition of the down-going plate ([Swenson and Beck, 1996](#); [Gutscher et al.,](#)
143 [1999](#); [Collot et al., 2004](#); [Agurto-Detzel et al., 2019](#); [Soto-Cordero et al., 2020](#); [León-Ríos et](#)
144 [al., 2021](#)) and the Ecuadorian forearc ([Collot et al., 2004](#); [Koch et al., 2020](#); [Lynner et al., 2020](#)).

145 In 2016, the Pedernales earthquake mainly ruptured two, ~ 20-30-km-deep locked patches
146 (P and J in Fig. 1b) while propagating southward ([Ye et al., 2016](#); [Nocquet et al., 2017](#)). Updip
147 of the Jama patch (J in Fig. 1b), the co-seismic rupture was arrested beneath the Cabo Pasado
148 shelf promontory by the ~ 10-15-km-deep, 50 x 50 km CP locked patch, centered ~45 km
149 landward from the trench. During the 30 days following the main shock, a large (60 cm) and
150 rapid after-slip developed at this patch, coincidentally with a remarkable after-shocks sequence
151 ([Rolandone et al., 2018](#); [Agurto-Detzel et al., 2019](#); [Soto-Cordero et al., 2020](#); [León-Ríos et al.,](#)
152 [2021](#)).

153 3. Data and Methods

154 3.1. Multibeam Bathymetric Data

155 The bathymetric map (Fig. 1c) is a compilation of swath bathymetry data collected during
156 the 2005 Amadeus and Esmeraldas cruises (RV L'Atalante), using a SIMRAD EM12D
157 multibeam system (13 kHz, 162 beams) ([Collot et al., 2005](#)). This data set was completed by
158 higher-resolution multibeam swath data collected on the shelf using SIMRAD EM122 (12 kHz,
159 288 beams) and EM710 (100 kHz, 256 beams) echosounders during the 2012 Atacames cruise
160 (RV L'Atalante) ([Michaud et al., 2015](#)). The RV L'Atalante bathymetric data were processed
161 using the CARAIBES software (IFREMER). The whole data set allowed constructing a
162 uniform digital elevation model with a 30-m grid spacing, using the nearest neighbor algorithm
163 of the GMT software ([Wessel and Smith, 1998](#)).

164 3.2. Multi-channel Seismic Imaging and Chirp data

165 A grid of Multichannel seismic reflection data was acquired during the 2009 Scan and 2012
166 Atacames cruises (Fig. 1c). Scan data were recorded using a 4000-in³ (65.5 L), 20- to 80-Hz
167 frequency air gun seismic source, and a 640-channel, 8-km-long digital streamer. Shots were
168 fired every 25 m, providing a 160-fold coverage. Scan data were processed by SINOPEC

169 (China Petroleum and Chemical Corporation) for PetroEcuador through classical steps
170 ([Yilmaz, 2001](#)), including multiple elimination, spherical divergence compensation, predictive
171 deconvolution in the Tau-P domain, prestack noise attenuation, stacking, and prestack time
172 migration. Atacames high-resolution seismic reflection data were recorded using a 72-channels,
173 450-m-long digital streamer. The source array consisted of two 13/13 in³ plus two 24/24 in³
174 mini-GI (Generator-Injector) guns, providing a signal with a peak frequency at ~130 Hz. Shots
175 were fired at 140 bars every 25 m ensuring a nine-fold stack. The seismic lines were processed
176 on board with the Seismic Unix software (Center of Wave Phenomena, Colorado School of
177 Mines) for band pass filtering, spherical divergence correction (water velocity), NMO (normal
178 moveout) velocity analysis and correction, stack and constant velocity-time migration (1,490
179 m/s). Sub-bottom profiler (Chirp), 1.8-5.3 kHz reflection data were acquired with a IXSEA-
180 DELPH system coincidentally with most Atacames seismic reflection lines.

181 182 3.3. Core data

183 Seven 0.88- to 2,44 m-long sediment piston cores recovered in the study area (Fig. 1c) using
184 a Kullenberg-type corer were analyzed for lithology, paleoenvironment, biostratigraphy, and
185 ¹⁴C dating.

186 4. Results

187 4.1. A Tectonic Map of the Cabo-Pasado continental shelf

188 We derive a tectonic map of the shallow-water (<125m) Cabo Pasado shelf promontory and
189 adjacent Bahia-Jama shelf basin, which southwest depocenter (SWBJ) lies in a margin slope
190 re-entrant under 300-600 m of water depth (Fig. 1c). The map shows that the axis of the
191 Pliocene-lower Early Pleistocene Bahia-Jama basin ([Hernández et al., 2020](#)) crosses the upper
192 margin slope, extends along the shelf and connects northward to the Pedernales basin (Fig. 3).
193 In contrast, the Pleistocene SWBJ depocenters ([Hernández et al., 2020](#)) are interrupted over the
194 shelf promontory by a broad composite anticline structure, where deformed Pliocene to lower
195 Early Pleistocene and Middle Pleistocene sediments crop out at the seafloor in water depth
196 locally shallower than 100 m (Fig. 3). The map also reveals three main sets of faults and
197 remarkable anticlines: (1) the 45 km-long N40-45°-trending, Bahia-Jama fault system (BJ) that
198 is segmented into i) the South Bahia-Jama fault (SBJ) that cuts through the SWBJ depocenter,
199 ii) the Central Bahia Jama fault (CBJ) and its associated braided pattern of anastomosing faults
200 (A1 to A6) that crosscuts the shelf edge; iii) the North Bahia-Jama fault (NBJ) that terminates
201 northeastward across the shelf promontory; (2) the N66°-70°E-trending, 5-18 km-long crustal
202 faults including the Cabuyal fault (Cab) that cuts the inner shelf promontory, and (3) the EW-

203 trending, ~20 km-long, North and South Canoa faults (SCa and NCa) across the SWBJ
204 depocenter, (4) the N to NE-trending San Vicente anticline which accommodates the transition
205 between the CBJ and NBJ fault segments, (5) the EW-trending Cabo Pasado anticline across
206 the shelf promontory, and (6) the NE-trending Canoa Anticline, which stands astride the upper
207 margin slope and shelf promontory.

208 4.2. A Crustal Transect across the offshore Bahia-Jama margin wedge

209 Deep penetrating line SCAN 900 (Fig. 2) cuts across the outer margin wedge from the
210 trench to the shelf edge, and the inner wedge further landward, thus revealing the broad scale
211 structure of the margin wedge and the relationship between the BJ fault system and the plate
212 interface. The plate interface is interpreted at the depth where frontal thrust faults appear to sole
213 out on a more continuous reflective sequence, as well as from intervals of strong reflections
214 between 4 and 6 stwtt (second two-way travel time) (~8 and ~16 km) depths, although they
215 may reflect under-plating making uncertain the actual location of the megathrust. Line SCAN
216 900 shows the CBJ fault segment to belong to a flower structure ([Hernández et al., 2020](#)) that
217 cuts steeply into the margin basement. The fault system projects downward to the megathrust,
218 thus isolating an outer-wedge tectonic sliver from the bulk of the margin. Based on SIS-58
219 crustal transect (see Figure 4 of Collot et al. (2004), the East-trending, SCa fault system
220 similarly cuts through the entire margin wedge. Both systems were interpreted as transtensional
221 strike-slip faults whose sustained activity controlled the Pliocene-Pleistocene sediment filling
222 of the 2-3 km-thick Bahia-Jama basin ([Collot et al., 2004](#); [Hernández et al., 2020](#)). The inferred
223 strike-slip mode of the BJ fault system is supported by the 47-52° obliquity between the plate
224 motion direction (N83°E) ([Nocquet et al., 2014](#)) and the normal to the fault system (N130-
225 135°E), which, in turn, predicts right-lateral slip (Fig. 1c). The quick disappearance of the fault
226 system towards the northeast suggests that only a limited trench-parallel translation of the outer-
227 wedge sliver was achieved, thus representing a very small fraction of the Ecuador large-scale
228 partitioning (Fig. 1a) ([Pennington, 1981](#); [Nocquet et al., 2014](#)).

229 4.3. Seismic stratigraphy of the Pleistocene sedimentary cover

230 Investigating the faults' structural style, and estimating the age of their activity and the
231 vertical motions of the margin wedge are instrumental to identifying temporal changes in the
232 megathrust behavior. This target requires scrutinizing the sedimentary architecture and dating
233 the shelf and upper slope deposits.

234 Two seismic stratigraphic packages separated by remarkable regional unconformity Uc
235 (noted U5 in Hernández et al. (2020)) are interpreted. The lower package encompasses units
236 L3a and L3b (Fig. 2) interpreted as well-stratified, tectonically deformed Pliocene to Lower

237 Pleistocene shelf basin deposits ([Hernández et al., 2020](#)). The upper package consists of
238 reflective and well-stratified, 0.05-0.55 stwtt (~37-410 m) -thick, seismic units 1, 2 and 3 that
239 are separated by regional unconformities Ua and Ub (Fig. 4, 5, 6). Units 1, 2 and 3 are composed
240 of a stack of elementary seismic sequences. In the SWBJ depocenter, ten elementary sequences
241 were picked up in Unit 1 (UTR 1 to 10), five in Unit 2 (MTR A to E), and 19 in Unit 3 (LTR F
242 to X) (Fig. S1 and 4). Assuming that climato-eustasy was the main driver of the changes in
243 accommodation space at 100- and ~40-ka time scales during the Pleistocene ([Vail et al., 1977](#);
244 [Embry, 1993](#); [Proust and Chanier, 2004](#)), the elementary seismic sequences correspond to
245 Transgression-Regression (T-R) sequences whose bounding unconformities tied to the well-
246 dated transitions between the even and odd marine isotopic stages (MIS) ([Lisiecki and Raymo,](#)
247 [2005](#)) provide a time frame for the sediment deposition in the study area (supporting text S1
248 and Table S1).

249 A biostratigraphic age control based on planktonic and benthic foraminifer assemblages
250 was performed on samples of all piston cores collected in the survey area (Fig. 1c). The analysis
251 provides a Late Pliocene to Pleistocene or Holocene age range for most samples (supporting
252 text S1 and Table S2; Popescu (2021)). Additionally, sedimentary core KAT25 collected along
253 line 46-1 (Fig. 6-I) provided a ^{14}C age of 46400 cal yr BP and potentially sampled the
254 unconformity between sequences UTR 8 and 9 (Fig. S3). Considering several sources of error
255 presented in supporting text S1, the potential ages derived for regional unconformities Ua, Ub
256 and Uc are 790 ka +/-110, 1031 ka +/-150, and 1832 ka +/-200, respectively. These ages were
257 simplified throughout the text and figures as 0.79, 1.0, and 1.8 Ma. The analysis of the internal
258 sedimentary architecture of the upper package has allowed recognition of Quaternary T-R
259 sequences that are used as a geological time frame to date the tectonic deformation.

260 4.4. Faulting and folding activity

261 4.4.1. Faulting activity

262 The BJ fault system does not have a modern seafloor expression. Instead, in many places,
263 the fault system shows a buried, 75-360 m-high, paleo fault scarp blanketed by 35-150 m of
264 undisturbed sediment (Fig. 4, 7, S1) advocating the present-day fault inactivity.

265 The South Bahia-Jama fault (SBJ) normally offsets unconformity Uc, indicating that the
266 fault ending postdates Uc. In the SWBJ depocenter, seismic lines ATAC-51 and SCAN-888
267 (Fig. 4, S1) show unconformity Uc to have acted as a growth normal fault, a fault that forms
268 contemporaneously with sediment deposition, as supported by the fan pattern of unit 3, the
269 bedding of which laps onto unconformity Uc. The growth fault is interpreted on seismic lines
270 of different orientations (Fig. 1c) revealing that extension with a ~NS component occurred near

271 the southern termination of the BJ fault system. In a strike-slip fault environment, this structure
272 can be viewed as a single releasing bend according to the terminology by Mann (2007). The
273 structure, which is bounded at the bottom and top respectively by unconformity U_c and U_b,
274 was mainly active from ~1.8 to ~1 Ma, as was the associated SBJ fault system (Fig. 4).

275 Late shortening affected the growth sequence as indicated by unit 3 internal folding
276 associated with branching fault A1 (Fig. 4). Such shortening on a branching fault succeeding
277 to growth faulting argues for a strike-slip component along the SBJ fault. The ultimate
278 shortening terminated with Unconformity U_b, thus pointing the primary ending of the SBJ fault
279 ~1 Ma ago, although residual deformation and auxiliary faults remained active up to
280 unconformity U_a dated ~790 ka (Fig. 4, 8). The ~320/360 m normal offset measured on the
281 SBJ fault scarp in line SCAN 888 (Fig. S1) occurred between unconformity U_c and U_b over
282 ~790 ka providing a mean vertical displacement rate of 0.4-0.45 mm/yr. The growth sequence
283 of Unit 3 is inferred to have recorded T-R sequences, as well as the integrated fault slip that
284 resulted from co-seismic increments of the fault growth and the SBJ fault scarp development,
285 although both controls on sedimentation cannot be disentangled.

286 The Central Bahia-Jama fault (CBJ) is part of the flower structure identified in crustal
287 section SCAN 900 (Fig. 2). CBJ is associated with a remarkable pattern of stratal deformation
288 in which, L3b reflectors from both sides of the fault dip asymmetrically towards the fault where
289 they are truncated (Fig. 7) and Hernández et al. (2020)). Although fan patterns associated with
290 branching faults A2 and A3 in line SCAN 900 (Fig. 2) show evidence of extension during L3b
291 deposition (Hernández et al., 2020), the bulging of the units L3a and L3b jammed between CBJ
292 and A2 faults argues for a late shortening phase. Altogether, these observations confirm strike-
293 slip along the CBJ fault. The CBJ fault scarp primarily resulted from repeating ruptures that
294 preceded the scarp erosion by unconformity U_c (Fig. 7, 6, 2). The bedding of unit 3 laps onto
295 the CBJ fault scarp, supporting that the fault activity had ceased by U_c, ~1.8 Ma ago (Fig. 8).

296 Branching faults A2 to A6 are short in map view and distribute extensional deformation
297 across the fault network (Fig. 3). According to Chirp data (Fig. 5d), faults A4 and A5 deform
298 the seafloor and the ~14-ka-old UTR 10 sequence, suggesting a recent activity (Fig. 8).

299 The North Bahia-Jama fault (NBJ) vanishes near the Cabo Pasado Anticline (Fig. 3). The
300 NBJ fault is blind on seismic lines ATAC-59, 61 and 62 (Fig. 7, 9, 10) and buried beneath ~
301 300 m of unit 1 sediment on line ATAC-59 (Fig. 7), whereas branching faults B1 and B2 crop
302 out at the seafloor in lines ATAC-61 & 62 (Fig. 9, 10). Comparing the structural configuration
303 of post-U_c units on lines ATAC-59 and 61 helps date the recent outer shelf deformation and
304 the ending of the NBJ fault activity. Both lines reveal a remarkable marker of the deformation,

305 which is a poorly reflective layer interpreted as a ~75 m-thick Mass Transport Deposit (MTD)
306 based on its poor reflectivity and strata truncated along its basal surface in line ATAC-59 (Fig.
307 7). On line ATAC-59, the MTD accumulated in a syncline flanked by the Canoa and San
308 Vicente anticlines, implying that shortening predated the MTD. The wavy shape of its section
309 further argues for the post-MTD continuation of the shortening. On line ATAC-61, the syncline
310 was inverted into an anticline, denoting the northward propagation of the San Vicente anticline,
311 leading to the truncation of UTR1 strata at the seafloor (Fig. 9c). On line ATAC-61, UTR1
312 strata thicken substantially seaward implying that a depocenter developed farther trenchward
313 during a short subsidence between 790 and 712 ka. Instead of thickening seaward, the lower
314 strata of overlying sequence UTR2 (Fig. 9c) thickens landward so that the age of this reversal
315 allows dating the propagation of the San Vicente anticline and, on the whole, the resumption of
316 the outer-shelf shortening and uplift, to lower UTR 2 deposits, likely between 712 and 676 ka
317 (Table S1). The timing of subsidence and subsequent uplift are further confirmed farther north
318 in line ATAC-65, where both a seaward thickening of UTR1 strata and a reversal of
319 stratigraphic divergence during the deposition of UTR2 lower strata are also documented (Fig.
320 S4c).

321 The end of the NBJ Fault and fault B1 activities can as well be estimated from seismic lines
322 ATAC-59 and 61 (Fig. 7 & 9), where the faults normally offset the MTD by ~50-55 m. The
323 upthrown section of the MTD was truncated by unconformity Ua, which, on line ATAC-59, is
324 slightly offset by fault NBJ. The fault was sealed by UTR1 early deposits implying that the
325 fault ended during the ~790-712 ka time interval. In line ATAC-61 (Fig. 9c), the upthrown
326 section of the MTD is truncated by Unconformity Ua, which, in turn, was shifted vertically by
327 a few meters across fault B1. The fault tip is associated with a 3-m-high seafloor bump (Fig.
328 9d) that could result either from a recent fault reactivation or from differential erosion. Several
329 seabed irregularities associated with un-faulted, tilted beds elsewhere along line ATAC- 61
330 (Fig. 9d) appear to result from erosion of beds of variable hardness, suggesting a similar origin
331 for the bump associated with fault B1, which is thus considered inactive, as already evidenced
332 on line ATAC-59 (Fig. 7). Therefore, the NBJ fault system likely ceased activity ~790-712 ka
333 ago, during the subsidence period and shortly before a new shortening and uplift phase began
334 affecting the shelf promontory 712-676 ka ago (Fig. 8).

335 The Cabuyal Fault (Cab) is blind and normally offsets unit L3b by ~50 m (Fig. 10). The
336 fault-created topography in unit L3b was eroded by unconformity Ua. However, the regional
337 stratigraphic correlation indicates that unconformity Ua is locally overlain by ~40 m of UTR2
338 deposits dated ~712 ka (Fig. 10), suggesting that the Cab fault activity could have stopped at

339 any time during the ~1 Ma-long hiatus defined between unconformity U_c, which truncated unit
340 L3b ~1.8 Ma ago, and the oldest UTR2 deposits (Fig. 8). Due to its location and trend, the Cab
341 fault is likely to be associated with the offshore projection of a strand of the onshore Jama fault
342 system (Fig. 3) ([Reyes and Michaud, 2012](#)).

343 The North and South Canoa faults (NCa, SCa) bound an EW-elongated and buried paleo-
344 basement high topped by a strong reflector (Fig. 11 and 2). The reflector is remarkably smooth
345 and contrasts with its elsewhere jagged appearance indicating that the basement high was
346 heavily eroded. The erosion occurred during the probable emergence of the basement high at
347 the Miocene-Pliocene boundary (~5 Ma) as inferred from its L3a sedimentary cover tentatively
348 dated Pliocene by Hernández et al. (2020). The Canoa faults, which have controlled the vertical
349 motions of the basement high, share a similar EW trend with a set of Oligocene to early middle
350 Miocene normal faults imaged offshore Cabo Pasado by Hernández et al. (2020), indicating
351 that they might be co-genetic. The NCa and SCa faults show, however evidence for strike-slip
352 motion. The SCa fault is correlated with a deep-seated flower structure (see Fig. 4 of Collot et
353 al. (2004), which shows poor evidence of activity since unconformity U_a, i. e., ~790 ka (Fig.
354 11). The NCa fault is associated in map view with the small Canoa ridge, where deformed
355 Paleogene to Miocene rocks (Fig. 3) crop out at the seafloor ([Hernández et al., 2020](#)). The ridge
356 consists of two en-échelon segments that trend ENE, oblique to the fault trend (Fig. 3) implying
357 a dextral component of strike-slip deformation. Line SCAN 417 (Fig. 11) does not show
358 evidence for post-790 ka NCa fault reactivation. However, further west along the NCa fault,
359 sediments of Unit 1 are faulted and bulge upward over the buried part of the ridge (Fig. 5)
360 indicating that tectonic deformation occurred since unconformity U_a ~790 ka. Chirp data (Fig.
361 5c) show sequences UTR8 and 9 to be faulted and folded suggesting that the NCa fault activity
362 continued until ~57 ka, and possibly up to 14 ka as indicated by UTR10 faint, diverging
363 reflectors evoking sedimentary progradation at the toe of the slope (Fig. 5c).

364 4.4.2. Folding activity

365 The San Vicente anticline initiated during the late shortening that deformed the lower
366 package (units L3a and b) of sediment between A2 and CBJ faults in line SCAN-900 (Fig. 2).
367 This shortening generated a transpression push-up, which locally inverted the Bahia Jama basin.
368 Although folding appears to have ended by unconformity U_c on line SCAN-900, synchronously
369 with the stopping of CBJ fault, the growth of the San Vicente anticline continued immediately
370 north, after unconformity U_c, as exemplified on lines ATAC-59 and 61 (Fig. 7 and 9). Indeed,
371 the stratigraphic analysis of line ATAC-59 (Fig. 7) indicates that the anticline grew at least up
372 to ~130 ka (UTR8) as substantiated by: i) the upward bulging of UTR sequences over the

373 anticline, ii) the progressive seaward migration of their depocenters, and iii) the disruption by
374 normal faults within the anticline of regional unconformities as young as the base of T-R
375 sequences UTR4 (533 ka) and UTR8 (130 ka) interpreted as former hard grounds (Fig.7c, 8).

376 The Cabo Pasado Anticline developed immediately north of the ending of the BJJ system
377 (Fig. 3). The analysis of Line ATAC-46-1 (Fig. 6) allows documenting the anticline's growth
378 and the shelf promontory's vertical motions. The southward-diverging pattern of UTR1 and
379 UTR 2 strata indicates that a small depocenter and correlative subsidence had developed in the
380 region of the Cabo Pasado Anticline over the 790 -621 ka time period. Normal fault N that
381 offsets the anticline by ~ 45 m (Fig. 6) was sealed during UTR1 deposits as indicated by a
382 neighboring SCAN profile (Fig. 5b in Hernández et al. (2020) suggesting that the fault activity
383 stopped during the subsidence period. Unit 1 sequences also recorded a recent phase of the
384 anticlinal growth. The unconformity at the base of sequence UTR3 separates the southward-
385 diverging strata of UTR1 and UTR 2 sequences from overlying, northward-diverging strata of
386 UTR3 (Fig. 6c), allowing to dating the shortening phase initiation to the early deposits of UTR3,
387 *i. e.* to ~621 -563 ka. The base of sequences UTR4 and UTR8 potentially identified on Chirp
388 data (Fig. 6-Id) is tilted northward and truncated at the seafloor, implying that the anticline
389 growth continued at least until ~130 ka (Fig. 8).

390 The Canoa Anticline (Fig. 7, 9) severely deforms units L3b and older units, seaward of the
391 NBJ fault. Line ATAC-59 (Fig. 7) shows that unconformity Uc was jointly deformed with the
392 L3b strata involved in the anticline, prior to being truncated by unconformity Ua, suggesting
393 that folding climaxed sometimes during the ~ 1-Ma-long sedimentary hiatus tentatively dated
394 between ~1.8 and 0.79 Ma over the anticline. Additionally, most normal faults that have
395 developed across the hinge of the anticline do not offset unconformity Ua, and this erosional
396 surface is gently overlain by undeformed sequences of unit1, arguing that the fold is no longer
397 active (fig. 7).

398 5. Discussion:

399 The results presented above reveal the timing of specific steps of the cumulative
400 deformation of the margin wedge offshore Cabo Pasado. In the discussion, we explore the more
401 suitable conditions of the long-term plate coupling that best account for specific steps of the
402 deformation and lead to the CP and J geodetically locked patches.

403 5.1. An outer-wedge, long-term inter-plate coupling prior to ~1.8 Ma

404 In oblique convergence settings, strike-slip faulting is a response to strain partitioning
405 when the megathrust accommodates trench-normal slip, and a trench-parallel margin fault takes
406 up the lateral component of slip (Fitch, 1972). This process leads to the formation of a forearc

407 sliver that moves along the margin ([Jarrard, 1986b](#)) as long as it is not opposed by a buttress
408 related to geometrical or inter-plate frictional conditions ([Beck et al., 1993](#)). Strike-slip faulting
409 often occurs along the volcanic arc because thermal softening makes it the weakest part of the
410 overriding plate ([Beck, 1983](#)). Trench-subparallel, strike-slip faulting is further documented
411 closer to the trench, in accretionary wedges e.g., along the Puerto-Rico ([ten Brink and Lin,
412 2004](#)), and southern Ryukyu trenches ([Lallemand et al., 1999](#)), and in fore-arc basins e.g., along
413 the Mentawai fault zone offshore Sumatra ([Diament et al., 1992](#); [Berglar et al., 2008](#)). In
414 addition to the convergence obliquity, which is a necessary condition met in our study zone,
415 the dominant factors controlling strain partitioning stand as the plate coupling, and a low
416 strength zone or mechanical heterogeneity in the margin wedge ([Jarrard, 1986b](#); [McCaffrey,
417 1992](#); [Chemenda et al., 2000](#); [McCaffrey et al., 2000](#)). Indeed, the outer-wedge, long-term plate
418 coupling must exceed the strength of the strike-slip fault to drag the fore-arc sliver effectively
419 along the trench.

420 Offshore central Ecuador, wide-angle seismic data ([Graindorge et al., 2004](#)) and local
421 earthquake tomography ([León-Ríos et al., 2021](#)) suggest that the nature of the margin's
422 basement is consistent with oceanic terranes similar in petrology to the late Cretaceous to
423 Paleocene basement rock that outcrops onshore ([Baldock, 1983](#); [Luzieux et al., 2006](#); [Jaillard
424 et al., 2009](#)). The Bahia-Jama and Canoa fault systems are believed to cut through the entire
425 oceanic basement (Fig. 2), Collot et al. (2004). They trend respectively ~NE and E-W, sub-
426 parallel to regional faults ([Reyes and Michaud, 2012](#)) known onshore to be ancient faults that
427 bound or cut through accreted oceanic blocks ([Luzieux et al., 2006](#)), thus pointing to
428 mechanically weak, inherited faults prone to be re-mobilized in a well-oriented stress field
429 ([Agurto-Detzel et al., 2019](#)). The consideration that the convergence obliquity remained high
430 over the last millions of years ([Somoza and Ghidella, 2012](#)), and that the BJ strike-slip fault
431 was active allows inferring that the shallow megathrust was coupled beneath the outer-wedge
432 tectonic sliver.

433 The 75-360-m-high paleo-scarp and the growth faulting associated with the activity of
434 the South and Central Bahia-Jama Fault segments prior to about 1 Myr are considered evidence
435 for large earthquakes to have produced repeated paleo-seafloor ruptures along the fault system
436 such as interpreted for Holocene splay fault seafloor scarps in Southern Prince William Sound,
437 Alaska ([Liberty et al., 2019](#)). Such inferred BJ fault paleo-seafloor ruptures also support local
438 plate coupling.

439 The inception of the BJ Fault system can be documented as well. As observed in
440 worldwide examples of large-scale buttressed fore-arc slivers controlled by a margin parallel

441 strike-slip fault ([Jarrard, 1986a](#); [Wang, 1996](#)), the Cabo Pasado anticline denotes trench-parallel
442 compression at the leading edge of the buttressed outer-wedge sliver, thus potentially relating
443 the anticline formation to the BJ fault system activity. Accordingly, the initiation of the anticline
444 during the late early Pliocene tectonic inversion of a local depocenter ([Hernández et al., 2020](#))
445 provides a clue for the timing of reactivation of the BJ fault system, and therefore the onset of
446 a relative, outer wedge plate coupling.

447 Plate coupling at the shallowest portion of the megathrust has been shown to be
448 consistent with seafloor geodetic observations offshore Peru ([Gagnon, 2005](#)), and Nankai
449 ([Yokota et al., 2016](#)) and with substantial shallow co-seismic slip during the Tohoku-Oki
450 earthquake ([Loveless and Meade, 2011](#)). Because the absence of off-shore geodetic data limits
451 the ability to resolve outer wedge inter-plate coupling, GPS data collected onshore Central
452 Ecuador allow a wide range of GPS models that consider either no or a medium inter-seismic
453 coupling west of the SBJ fault system ([Chlieh et al., 2014](#); [Gombert et al., 2018](#); [Rolandone et](#)
454 [al., 2018](#)). However, the past activity of the BJ fault system suggests that although non-
455 quantified, long-term, inter-plate coupling was permitted beneath the outer wedge sliver prior
456 to ~1.8 Ma.

457
458 5.2. The Cabo-Pasado and Jama locked patches: results of a local increased plate
459 coupling since ~1.8 Ma.

460 The abandonment of the BJ fault system was progressive as attested by the ~1.8 to 1 Ma,
461 limited ~ NS extension documented in the releasing bend, and the inferred latest deformation
462 along branching fault A1(Fig. 4). This abandonment could have resulted from an overall
463 reduction of the outer wedge inter-plate coupling, which became inefficient enough to prevent
464 slip partitioning. Alternatively, a relative increase of the inter-plate coupling focused beneath
465 the shelf promontory would have slowed down or even inhibited the translation of the outer-
466 wedge sliver as suggested by structural evidence in other regions ([Beck, 1983](#)).

467 According to physical and numerical models based on the Coulomb wedge theory
468 ([Lallemand et al., 1994](#); [Dominguez et al., 2000](#); [Ruh et al., 2013](#)), depending on the strength
469 and geometry of the wedge, subduction along a planar and weak megathrust produces less off-
470 fault margin deformation and topography than along a rough and strong plate interface where
471 the subduction deforms the margin wedge severely by shortening and uplift in the convergence
472 direction. In the region of the CP shelf promontory, the post- ~1.8 Ma tectonic history supports
473 the hypothesis of a relative increase in plate coupling. Indeed, the phase of shortening, which
474 succeeded the Pliocene -lower Early Pleistocene period of fore-arc basin subsidence recorded
475 by unit L3 deposits ([Hernández et al., 2020](#)), terminated by the uplift and vigorous erosion of

476 deformed unit L3b (Fig. 6). This phase peaked during the ~1.8-0.79 Ma sedimentary hiatus
477 outlined by unconformity Ua on the shelf promontory (Fig. 8). Additionally, the shallowness
478 of unconformity Ua suggests that the shelf promontory emerged during early Pleistocene sea-
479 level lowstands ([Hansen et al., 2013](#)). Subsequently to its emergence and severe erosion, the
480 whole shelf promontory subsided over the 790-712 ka time gap before uplift and landward tilt
481 resumed during the 712-621 ka time interval, as interpreted from UTR1 and 2 internal
482 architectures at both extremities of the shelf promontory (Fig. 9 and S3). Uplift of the whole
483 shelf promontory proceeded after 621 ka as indicated by the southward progradation of
484 sequences younger than UTR2 (Fig. 6), as well as by the northward (Fig. 6) and landward (Fig.
485 S4) migration of the depocenters of these sequences. The deformation amplified locally with
486 the resumption of the growth of the Cabo Pasado anticline over the 621-533 ka time gap as
487 interpreted from UTR3 internal deposits (Fig. 6 c). Overall, this new phase of deformation
488 caused unconformity Ua and younger strata of the shelf promontory to be truncated at the
489 seafloor during high-amplitude (~120 m), Middle to Upper Pleistocene low sea level stands
490 ([Miller et al., 2005](#); [Hansen et al., 2013](#)), while over areas of the inner shelf, sedimentation
491 proceeded since UTR3, in the form of condensed sequences. In our data set, disrupted hard
492 grounds and tilted beds as young as 130 ka (UTR8), 57 ka (UTR9) and possibly 14 ka (UTR10)
493 are the most recent traces of the ongoing tectonic deformation associated with the San Vicente
494 (Fig. 7c) and Cabo Pasado anticlines (Fig. 6-Id).

495 In conclusion, the shortening and uplift history of the shelf promontory, which had initiated
496 in the mid-early Pleistocene (~1.8 Ma) after a long period of subsidence, points to a major
497 change in the stress regime beneath the shelf promontory. The enduring shortening indicates
498 that the margin wedge has long been in a compressively critical state implying a long-term plate
499 coupling. The spatial correlation between the CP locked patch and the uplifted shelf
500 promontory, which has been deforming for a hundred thousand years (Fig. 12) indicates the
501 persistence of the long-term plate coupling until the present. The Cabo-Pasado and Jama locked
502 patches are therefore considered as present-day representatives of the long-term plate coupling.
503 This coupling could originate either from long-lived, high-basal friction ([Wang and Hu, 2006](#);
504 [Wang, 2010](#)), or a geometrical resistance to the fault motion due to a rugged subducting seafloor
505 ([Wang and Bilek, 2014](#)). Finally, our result points to long-term operating tectonic mechanisms
506 linking the megathrust mechanical behavior and the buildup of permanent fore-arc deformation
507 offshore central Ecuador.

508 5.3. Subduction of the Carnegie Ridge crest

509 5.3.1. A cause for the long- and short-term plate coupling in the Cabo Pasado
510 Area.

511 Subducting rough topography is believed to exert a strong control on the structural
512 development of convergent margins ([Dominguez et al., 2000](#); [Ruh et al., 2016](#)), although its
513 role in inter-plate coupling and seismogenesis is still disputed ([Wang and Bilek, 2014](#); [Bassett
514 and Watts, 2015](#); [Collot et al., 2017](#); [van Rijsingen et al., 2018](#)). In Ecuador, the relationship
515 between subducted CR and the fore-arc structure has long been pointed out ([Lonsdale, 1978](#);
516 [Gutscher et al., 1999](#); [Collot et al., 2004](#)). Due west of the study area, the crest of the eastern
517 CR consists of a ~40-60-km wide, volcanic basement swell with peaks barren of sediment,
518 which culminates at a ~650 m-water depth (Lonsdale, 1978). Although the seafloor morphology
519 prior to subduction may not fully reflect the inter-plate morphology, the residual bathymetry of
520 the Ecuador margin, which was obtained by subtracting an averaged topography from the
521 bathymetric grid, is highest over the outer wedge in our study zone and is interpreted to be due
522 to the subducted eastern CR (Agurto-Detzel et al. (2019).

523 In more detail, we consider that the conspicuous alignment along a N83°E-trending corridor
524 parallel to the plate convergence direction (Fig. 12) of (1) the shallowest Ecuadorian trench
525 segment, (2) a remarkable slump scar left in the outer wedge (Fig. 3), (3) the shallowest and
526 highly deformed shelf promontory, (4) the Cabo-Pasado and Jama locked patches, (5) the
527 highest 2016-co-seismic uplift (~51.4 cm) and greatest seismic moment released (Fig. 1b) in
528 the Jama-Cabo Pasado onshore area ([Nocquet et al., 2017](#)), and (6) the coastal exposure, west
529 of Jama city (Fig. 1b), of Upper Early Pleistocene inner-shelf to fluvial deformed sediment
530 ([Cantalamesa et al., 2005](#)) supports the hypothesis that the Cabo-Pasado and Jama locked
531 patches correlate with CP and J subducted reliefs of the CR crest. With respect to the 30 km NS
532 extent of the uplifted shelf promontory, a reasonable size for the footing of the reliefs would
533 range from 40 to 50 km. The subducted reliefs hypothesis seems reasonable as the Cabo Pasado
534 shelf promontory shares similar characteristics of inter-seismic coupling level and depth, slow-
535 slip mode ([Rolandone et al., 2018](#)), bathymetry and tectonic history with the La Plata area
536 ([Proust et al., 2016](#)) (Fig. 1a), the locked patch of which is caused by a subducted oceanic relief
537 of the CR ([Collot et al., 2017](#)). According to this hypothesis, the CP and J locked patches would
538 rather be caused by an irregular geometry of the plate inter-face than only by patches of high-
539 basal friction. Indeed, the CP-locked segment of the megathrust is considered relatively weak
540 as it slipped aseismically after the 2016 event and was the site of three slow-slip events (SSEs)
541 since 2010 ([Rolandone et al., 2018](#)). The geometrical resistance interpretation suggests that the
542 locked patches did not remain stationary but instead moved along with the subducted reliefs.

543 5.3.2. A Subduction scenario for the CR crest

544 To further test the subducted reliefs hypothesis, we tentatively reconstructed their past
545 geographic positions and compared them with the main stages of the margin wedge sequential
546 deformation. The subduction rate of the reliefs (V_r) equals the inter-plate shortening rate ($V_{gps} =$
547 4.7 cm/yr) minus the shortening rate of the margin wedge (V_s). Quaternary coastal uplift rates
548 were shown to represent $\sim 4\text{-}8\%$ of the modeled inter-seismic uplift rates in Northern Chili
549 ([Jolivet et al., 2020](#)). As shortening and uplift are related in our study zone, V_s could similarly
550 be considered one order of magnitude lower than V_{gps} . V_s sums up the horizontal tectonic
551 shortening estimated from the seismically imaged structures, and diffuse strain caused by
552 pervasive small-scale faulting, loss of porosity and ductile deformation ([Adam et al., 2004](#)).
553 With the exception of a few thrust faults at the toe of the margin, no major thrust fault was
554 imaged deforming the margin wedge since ~ 0.79 Ma in the promontory area (Fig. 2). In
555 contrast, some seismic sections allow estimating that permanent folding across the shelf
556 promontory has accommodated ~ 550 to ~ 900 m of shortening since ~ 0.712 Ma providing a
557 0.08 to 0.12 cm/yr shortening rate (i. e. $\sim 1.7\text{-}2.6\%$ of V_{gps}). Since diffuse strain, which is
558 assumed to be $\sim 5\text{-}10\%$ in deformed sediment of the Cascadia frontal accretionary wedge ([Adam](#)
559 [et al., 2004](#)), is unknown in the fractured basement of Ecuador, and that tectonic shortening by
560 faulting and folding is estimated in the order of $2\text{-}3\%$, we consider V_s to be at most 10% $V_{gps} =$
561 0.47 cm/yr implying $V_r = V_{gps} - V_s = 4.23$ cm/yr. This rate is used to calculate the position of the
562 center of the two reliefs at several ages along a time line trending $N83^\circ E$ (Fig. 13).

563 Because these time-related positions were obtained independently of the ages of
564 unconformities U_a , U_b and U_c , the kinematic model in Fig. 13 is considered significant within
565 the limits of the uncertainties on both V_s and the sequential stratigraphy. In this model, relief J
566 underthrusts the outer wedge at ~ 1.8 Ma, rising the inter-plate coupling locally, thus
567 contributing to blocking the BJ Fault system. At ~ 1 Ma, both reliefs J and CP underthrust the
568 margin wedge increasing the margin normal stress and inter-plate coupling along the entire
569 corridor, uplifting the shelf promontory and freezing the BJ fault system. Between 0.8 and 0.6
570 Ma, the in-sequence subduction of relief CP and of a speculated saddle between reliefs J and
571 CP, could account for the short subsidence period ($\sim 790\text{-}712$ ka) of the shelf promontory,
572 followed by its renewed uplift from ~ 712 ka. In this scenario, the ~ 100 m-thick, upper Early
573 Pleistocene marine to fluvial deposits exposed along the coast west of Jama city ([Cantalamessa](#)
574 [et al., 2005](#)) would have started uplifting after ~ 1 Ma with a ~ 0.1 mm/yr mean uplift rate.
575 Additionally, the morphologic scar left in the outer wedge would have formed from ~ 790 ka,
576 on the trailing flank of relief CP according to models by Dominguez et al. (2000).

577 5.3.3. Effect on the Mw 7.8 2016 earthquake rupture

578 Our kinematic model is consistent with the subduction in a row of two reliefs, of which
579 relief CP is buried at a ~10-15 km depth beneath a faulted margin wedge, and relief J at a ~25
580 km-depth in a higher-stress environment. The latter is supported by the high and localized
581 moment released at the J relief during the Mw 7.8, 2016 earthquake ([Nocquet et al., 2017](#)). The
582 J relief did not trigger the event, which initiated farther north, nor did it fully stop the southerly
583 spread of the rupture, since a ~1 to 2 m co-seismic slip ([Nocquet et al., 2017](#); [Gombert et al.,
584 2018](#)) propagated over a ~25-30-km distance south of the presumed location of relief J.
585 Although the shape and size of relief J are unknown, the earthquake rupture segment boundary
586 could be dominantly controlled by the major along-strike change of the margin basement
587 seismic properties documented by Lynner et al. (2020).

588 In contrast with the stick-slip frictional instability at relief J, the large 2016-after slip at
589 relief CP (Fig. 12) testifies to the up-dip damping of the rupture propagation, which prevented
590 unzipping the whole megathrust up to the trench. The damping reflects either a weak
591 accumulation of stress in that area because of the recurrent SSEs ([Rolandone et al., 2018](#)) or a
592 decrease in rigidity of the lower part of the margin ([Sallares and Ranero, 2019](#)), or a
593 combination of both. At a ~10-15-km-depth, relief CP underthrusts basement rocks with ~5.5
594 km/s Vp velocity, a value lower than the 6.5 km/s of the margin rocks at 20-25 km depth near
595 relief J (Profile 7, Fig. 7 in León-Ríos et al. (2021)). Such Vp drop supports a reduced rigidity
596 of the foundation of the margin wedge above relief CP. Fluid circulation associated with
597 increased fracturing related to past subduction of other reliefs could be responsible for the loss
598 of rigidity. Besides, a weak subduction channel and a fluid-driven damage of the underside of
599 the margin's mafic basement ([Sage et al., 2006](#)) might contribute to reducing both the margin-
600 basement rigidity and inter-plate friction, thus preventing seismic rupture. In the context of
601 subducted relief CP, this inference looks compatible with global studies stating that rough
602 subducting seafloor is associated with weaker plate coupling and is less prone to nucleate large
603 earthquakes than smooth subduction interface ([Lallemand et al., 2018](#); [van Rijnsingen et al.,
604 2018](#)). Yet, at relief CP, the margin rigidity seems to remain high enough for the irregular
605 geometry of the megathrust to resist shear motion, accumulate some elastic strain and hold
606 locked the CP patch, until it fails during episodic SSEs or after-slip. In this view, the CP relief
607 and physical properties of adjacent rocks could have impeded the generation of a significant
608 tsunami during the Mw7.8, 2016 earthquake. This interpretation, which seems relevant for the
609 mafic, nonaccretionary convergent margin of central Ecuador, contrasts with the proposal that
610 shallow SSE sources are conducive to tsunami earthquakes, especially when the sources are

611 associated with subducted seamounts as suggested on the Hikurangi accretionary margin ([Bell](#)
612 [et al., 2014](#); [Wallace et al., 2016](#)). However, although no historical tsunami earthquakes are
613 known offshore Cabo Pasado, it is possible that the shallow megathrust has not accumulated
614 enough elastic strain so far, but that it might do so in the future and produce a tsunami, as was
615 the case in Chili during the Mw 8.3, 2015 Illapel earthquake ([Melgar et al., 2016](#)).

616 5.4. A change in the mode of permanent deformation

617 Co-seismic surface ruptures preserved in the seafloor topography result from the inelastic
618 part of the deformation, as exemplified by Tsuji et al. (2013) about the rupture of the 2011
619 Tohoku-oki earthquake. In the study area, part of the permanent deformation of the margin's
620 wedge was likely acquired during large earthquakes, prior to 1.8 and up to 0.79 Ma when
621 segments of the BJF were active, as supported by: (i) well-preserved paleo-seafloor ruptures
622 across the major faults (Fig. 4, 7, 10), and (ii) the ~75 m-thick MTD and its sharp 50-55-m-
623 high vertical offset that presumably reflect repeated ruptures along the NBJ Fault segment (Fig.
624 7).

625 In contrast, as indicated by seismic reflection data, neither the Mw8.6-8.8, 1906, and Mw
626 7.8, 1942 megathrust earthquakes nor the Mw ~ 7, 1896, 1956, and 1998 thrust earthquakes
627 that occurred astride the creeping barrier ([Font et al., 2013](#); [Vaca et al., 2019](#)) were able to
628 reactivate the Bahia-Jama and Cabuyal fault systems to transfer detectable slip to the seafloor.
629 Rather, post-0.79 Ma shelf promontory deformation appears to have been controlled by gentle
630 folding, and secondary faulting as expressed by (i) the growth of San Vicente and Cabo Pasado
631 anticlines, which is documented at least until ~130 ka, and (ii) the activation of branching faults
632 A4-A5 and the North Canoa Fault documented up to ~14 ka and possibly to present, based on
633 seafloor morphology (Fig. 5, 8, 11). These observations mean that the stress field and inter-
634 plate behavior changed at some point from 0.79 Ma, inducing a remarkable modification of the
635 permanent deformation process.

636 Although multiple mechanisms occurring either deep or shallow along the plate interface
637 could contribute to the permanent deformation as discussed by Melnick (2016) about the central
638 Andean coast, transient aseismic slips and moderate size earthquakes might be the main drivers
639 of the post 0.79 Ma permanent deformation in the study area. The inter-seismic seismicity
640 ([Vaca et al., 2019](#)), the SSEs ([Rolandone et al., 2018](#)), the 2016-after-slip and after-shocks
641 sequence ([Rolandone et al., 2018](#); [Agurto-Detzel et al., 2019](#); [Soto-Cordero et al., 2020](#))
642 contribute to multiple faults activation and potentially to the fold growth. The 2016 after-shocks
643 include earthquakes thought to rupture the same seismic asperity repeatedly. [Chalumeau et al.](#)
644 (2021) found the repeating earthquakes to cluster near the plate interface. There, the alignment

645 of repeaters-broken seismic asperities along a slightly curved EW-direction (Fig. 12) might
646 reflect inter-plate structural complexities related to the northern flank of the subducted CP
647 relief. The modest \sim M3.0 of the repeaters ([Chalumeau et al., 2021](#)) and the Mw 3.2-6.0 of the
648 thrust events (Fig. 12) ([Rolandone et al., 2018](#); [Agurto-Detzel et al., 2019](#)) (Fig. 12) imply a
649 moderate off-fault deformation however. Interestingly, ten weeks after the 2016 main shock,
650 four Mw 3.6 to 4.6 earthquakes with strike-slip focal mechanisms happened to cluster at
651 shallow depths (8-14 km) ([León-Ríos et al., 2019](#)) along the NCa fault, pointing to its dextral
652 reactivation (Fig. 12). The fault rupture likely responded to the subduction of relief CP
653 according to the fault network model around a subducted seamount by Dominguez et al. (2000).
654 In addition to this recent fault reactivation, evidence of MTDs emplaced immediately south of
655 the NCa fault, (Fig. S5), indicates that roughly \sim 712 -621 ka ago, the region of the NCa fault
656 suffered from the brunt of earthquakes. Hence, the long-term reactivation of the NCa fault
657 contributed to accumulating permanent deformation and shape the Canoa ridge. Thus, we
658 suggest that since the sealing of the BJ and Cabuyal fault system, permanent deformation
659 accumulated primarily during the inter- and post- seismic periods, a similar situation as that
660 proposed by Victor et al. (2011) at the Mejillones Peninsula in Chili.

661 **6. Conclusions**

662 The Quaternary tectonic evolution of the nonaccretionary margin of Ecuador, offshore Cabo
663 Pasado (CP) shows that permanent fore-arc deformation resulted from an episode of strike-slip
664 tectonics followed by periods of severe shortening and uplift of the CP shelf promontory. This
665 evolution likely reflects a long-term, inter-plate coupling progression beneath the shelf
666 promontory. The coupling progression was marked by a drastic change in the mode of
667 permanent deformation from co-seismic deformation likely acquired during large earthquakes
668 prior to 1.8 and up to 0.79 Ma when the BJ system was active, to folding and secondary faulting
669 occurring during the post and inter-seismic periods since \sim 0.79 Ma. This finding suggests a
670 major change in inter-plate mechanical behavior from a stick-slip mode for several hundred
671 thousand years to a transient aseismic slip mode of similar duration.

672 The NNEward translation of an outer-wedge tectonic sliver along the Bahia Jama trench
673 parallel, strike-slip fault system prior to \sim 1.8 Ma implies that the megathrust was coupled
674 beneath the outer-wedge sliver. Within this view, active strike-slip faults might be regarded as
675 good evidence of significant near-trench coupling at nonaccretionary margins. This hypothesis
676 might be tested in the future as sea-floor geodesy experiments will provide new constraints on
677 the near-trench inter-seismic coupling.

678 The plate coupling increased strongly beneath the shelf promontory ~1.8 Ma ago, likely in
679 response to the subduction in a row of J (Jama) and CP reliefs of the Carnegie Ridge crest. After
680 a short, period of subsidence, this regime persisted until today in the form of the J and CP
681 geodetically locked patches. An implication of this finding is that the irregular geometry of the
682 subducting reliefs resisting shear motion plays a dominant role in the long- and short-term plate
683 coupling, at least for non-accretionary convergent margins.

684 In contrast with the J geodetically locked patch, which ruptured seismically during the
685 M7.8, 2016 event, the shallower CP locked patch was the locus of aseismic slip, and is
686 considered associated to a relatively weak megathrust segment. We suggest that the deepest
687 subducted relief J contributed to concentrating high-stress where the highest seismic moment
688 was released during the 2016 earthquake. Unlike, the shallowest relief CP had focused less
689 stress due to a combination of frequent SSEs and a reduced rigidity of the fractured outer-wedge
690 basement, thus impeding updip propagation of the rupture, and hence avoiding the triggering
691 of a significant tsunami during the 2016 event. Therefore, at non-accretionary convergent
692 margins, shallow subducted relief might be considered a natural obstacle to the formation of
693 devastating tsunamis

694 Overall, although it is essential to document the ISC coupling by geodesy, and critical to
695 investigate the physical conditions of the plate interface and adjacent rocks, the Quaternary
696 geological evolution of subduction margins provides additional constraints for understanding
697 the current inter-plate coupling and rupture processes.

698

699 **Acknowledgments and Data**

700 This work was carried out in the frame of the Joint French-Ecuador Laboratory
701 “Earthquakes and Volcanoes in the Northern Andes” and was funded by the Institut de
702 Recherche pour le Développement (IRD), the Institut National des Sciences de l'Univers
703 (INSU), and the Institut Français pour l'Exploitation de la Mer (IFREMER), which provided
704 ship time, equipment, and data processing during the Atacames cruise. We are grateful to the
705 Secretaria de Hidrocarburos del Ecuador (SHE) for providing us with seismic sections from
706 the SCAN-2009 seismic experiment within the framework of the SHE-IRD and SHE-EPN
707 cooperation agreements. We thank Schlumberger for offering the use of PetrelTM software.
708 Finally, we acknowledge two anonymous reviewers and the Associate Editor for their helpful
709 comments.

710 All data from the Atacames cruise used in this work are available at the French National
711 Marine Database SISMER following the link <https://doi.org/10.17600/12010010> (pages are in

712 French and in English). This includes seismic data stored under the folder “Data Managed By
713 SISMER” and « National Bank of Raw Marine Seismic Data ». The first set of files are Chirp
714 data, followed down the list by HR Seismic data. Seismic line number used in this publication
715 refers to the one used in the seismic data base. Data labeled « restricted access » will be made
716 available following a request via an Application Form on the platform after advice of the cruise
717 supervisor conformably to the European and French legislation. Requirement for SCAN-2009
718 seismic data can be addressed to Dirección de Análisis de Información Estratégica de
719 Hidrocarburos Av República de El Salvador N36-64 y Suecia, Quito 170135. Edificio MSP.
720 Piso 5, Ecuador.

721

722

723 Figures Captions

724 **Figure 1.** Geodynamic setting, bathymetry, inter-seismic coupling and location of seismic
 725 lines in the study area. (a) Geodynamic setting, red frame is location of Fig. 1b in Central
 726 Ecuador where Carnegie Ridge is subducting; red stars are 1906 to 2016 large to great
 727 subduction earthquakes. Dash ellipse is estimated rupture zone of the Mw 8.6-8.8, 1906
 728 earthquake (Kelleher, 1972). 47mm/yr is convergence rate between Nazca plate and North
 729 Andean sliver (Nocquet et al., 2014). LP= La Plata Island; (b) Inter-seismic coupling map
 730 (color bar 0-100%) with Pedernales (P), Jama (J) and Cabo Pasado (CP) locked asperities
 731 (Rolandone et al., 2018); White star is epicenter of the Mw 7.8, 2016 with white contours
 732 indicating co-seismic slip in meters. Dashed lines are estimated depth contours of the plate
 733 interface in km (Hayes et al., 2012). Black frame is location of Fig. 1c. (c) Multibeam
 734 bathymetric map with contours every 50 m, and 25 m on the shelf. White barbed line is the
 735 subduction trench; blue dotted line is shelf edge; white lines with tick marks are slope scars;
 736 thin red lines are SCAN seismic data; thin blue lines are ATACAMES seismic and chirp data
 737 (Michaud et al. 2015); SIS-58 is SISTEUR seismic line from Collot et al., (2004); bold
 738 segments with figure numbers are the seismic sections presented in the text and supporting
 739 information; yellow-orange pattern represents CP and J locked asperities; simplified fault
 740 pattern in red (see Fig. 3). KAT24 to 33 are ATACAMES coring sites.

741

742 **Figure 2.** Deep penetrating seismic reflection SCAN line 900 across the margin wedge
 743 offshore Cabo Pasado. (a) un-interpreted section with crossing seismic lines; (b) the line
 744 shows the outer wedge tectonic sliver, the Central Bahia Jama strike-slip fault segment (CBJ)
 745 and the megathrust; L1-L2 units =Middle Eocene to Late Miocene, and L3a-L3b units =
 746 Pliocene to early Pleistocene (Hernandez et al., 2020); Uc (light green) is major unconformity
 747 between lower and upper packages, and outlines the CBJ paleo fault scarp. Note that faults
 748 A2 and A3 recorded extensional deformation during unit L3b deposition. Strong reflector
 749 (dark green) shows the margin basement to be faulted by the CBJ-A2 fault system, and
 750 strongly eroded beneath the SW Bahia Jama depocenter; (c) map showing line location.

751

752 **Figure 3.** Structural and geological map of the study area. SBJ, CBJ and NBJ are South,
 753 Central and North Jama fault segments; Cab is Cabuyal fault; NCa and SCa are North and
 754 South Canoa faults. A1 to A6 are branching faults; Onshore lineaments = Jama fault system

755 (Reyes and Michaud, 2012); KAT24 to 33 are coring sites; Note the broad composite
 756 anticline structure associated with the shelf promontory where Late Pliocene- lower Early
 757 Pleistocene (light green) and Lower Middle Pleistocene (yellow) sediment outcrop at the
 758 seafloor in water depths less than 125 m. Thin blue lines are seismic and chirp data.

759
 760 **Figure 4.** Seismic reflection line ATAC-51 across the SW Bahia-Jama depocenter and A1-
 761 SBJ fault system (vertical red lines). (a) un-interpreted section with crossing seismic lines.
 762 Depth in stwtt (second two-travel time); VE= Vertical exaggeration; (b) interpreted section
 763 indicates Units 1, 2 and 3, major unconformities Ua, Ub and Uc and the fan shape structure of
 764 Unit 3. Dashed red line indicates that unconformity Uc was a growth normal fault (see text
 765 and Fig. S1). Names and lettering UTR 1-10, A to E and F to S within the units refer to
 766 elementary seismic sequences interpreted on line SCAN-888 (Fig. S1); thin red and orange
 767 lines are respective base of regionally interpreted elementary seismic sequences UTR4 and
 768 UTR8. Ages of major unconformities are determined on the basis of the sequential
 769 stratigraphy and piston core data (supporting text S1 and Table S1). (c) map showing line
 770 location.

771
 772 **Figure 5.** Seismic reflection line ATAC-57 and Chirp data across the SW Bahia-Jama
 773 depocenter, the western segment of the North Canoa (NCa) fault, and the A4 -A5 and Central
 774 Bahia-Jama fault segment (CBJ); (a) un-interpreted section with crossing seismic lines; (b)
 775 interpreted section (see Figure 4 for caption); (c) and (d) Chirp data showing latest sequences
 776 of Unit 1 (UTR 8-9-10) to be deformed respectively by the NCa fault; (c) and A4 and A5
 777 faults (d) (see text); (e) map showing line location.

778
 779 **Figure 6.** Seismic reflection line ATAC-46-1 and its continuation 46-2 from the Pedernales
 780 basin through the Cabo Pasado anticline and the shelf promontory to the SW Bahia-Jama
 781 depocenter; Top: (Ia) un-interpreted section with crossing seismic lines across the Cabo
 782 Pasado Anticline and Fault N; (Ib) interpreted section shows structures and inferred ages.
 783 Unconformities Ub and Uc are interpreted near the northern end of the line, whereas, Units 1
 784 and L3b outcrop at the seafloor respectively North and South of fault N; see Figure 4 for
 785 stratigraphy and ages caption. KAT 24, 25 and 29 are sedimentary cores with their length. (Ic)
 786 zoom imaging the northward diverging pattern of lower strata of sequence UTR3 (black
 787 double arrows beneath the red arrow) that opposes the southward diverging pattern of
 788 sequences UTR1 and 2, thus dating resumption of the anticline growth; (Id) Chirp data shows

789 that unit 1 sequences up to UTR 8 and 9, are tilted and truncated at the seafloor defining a
 790 sediment-bare morphology with subtle irregularities; (Ie) map showing the location of the two
 791 segments of line 46; Bottom : (IIa) un-interpreted section of line 46-2 with crossing seismic
 792 lines showing the geological structure across the Central Bahia-Jama fault system (CBJ); (IIb)
 793 interpreted section (see Figure 4 for Stratigraphy and ages caption). Note that Units 2 and 3
 794 are found only south of the CBJ fault implying a ~1 Ma-long hiatus on the shelf promontory
 795 (see Fig. 8). KAT30 is sedimentary core dated older than 50 ka.

796

797 **Figure 7.** Seismic reflection line ATAC-59 and Chirp data imaging both the North Bahia
 798 Jama (NBJ) / B1 fault and the Central Bahia-Jama fault segments (CBJ), as well as the Canoa
 799 and San Vicente anticlines. (a) un-interpreted section with crossing seismic lines; MTD =
 800 Mass Transport Deposit; (b) interpreted section (see Figure 4 for stratigraphy and ages
 801 caption). Unconformity Uc (light green) sealed the CBJ strike-slip fault and its paleo scarp,
 802 whereas NBJ /B1 faults were sealed near unconformity Ua (blue). Note the MTD laid in a
 803 syncline prior to be offset by NBJ fault and deformed by the growing San Vicente anticline;
 804 (c) Chirp data suggests that the shallow sequences of Unit 1 (UTR 4 and 8) are faulted above
 805 the San Vicente anticline. (d) map showing line location.

806

807 **Figure 8.** Chronostratigraphic correlation of Pleistocene units 1, 2, 3 and L3b deposits, and
 808 unconformities Ua, Ub and Uc along a strike section across the Cabo Pasado shelf
 809 promontory based on interpretations of NW-trending ATAC seismic lines (line numbers at
 810 top) and strike line ATAC 46 (Fig. 6); units color as in Figure 3; thick red bars: major fault
 811 activity (SBJ, CBJ, NBJ= South, Central and North Bahia-Jama fault segments, and faults B1,
 812 B2, fault N and Cab (projected Cabuyal Fault); thin red bars: A1-A5 branching faults activity;
 813 stars: last evidence of faulting activity from seismic or chirp data (black), from seafloor
 814 morphology (white); triangles: first (black) and last (white) evidence of uplift/fold growth;
 815 pale blue arrows= subsidence; green arrows= uplift; grey arrows: growth of San Vicente and
 816 Cabo Pasado anticlines.

817

818 **Figure 9.** Seismic reflection line ATAC-61 and Chirp data across the North Bahia Jama
 819 (NBJ) / B1 faults, and Canoa and San Vicente anticlines. (a) un-interpreted section with
 820 crossing seismic lines; MTD (Mass Transport Deposit); (b) interpreted section (see Figure 4
 821 for stratigraphy and ages caption). Note that the MTD identified in line ATAC-59 (Fig. 7),
 822 was inverted with the San Vicente anticline, and offset vertically by fault B1; (c) zoom

823 imaging the landward diverging pattern of lower strata of sequence UTR2 (thin black double
824 arrows beneath the red arrow) that opposes the trenchward diverging pattern of sequence
825 UTR1 thus dating the recent uplift of the outer shelf (see text); (d) Chirp data showing the
826 faulted apex of the San Vicente anticline and subtle (~3m) seafloor bump associated with
827 fault B1 and landward tilted UTR beds; (e) map showing line location.

828
829 **Figure 10.** Seismic reflection line ATAC-62 and Chirp data across the North Bahia Jama
830 (NBJ) / B2 and Cabuyal (Cab) faults. (a) un-interpreted section with crossing seismic lines;
831 (b) interpreted section (see Figure 4 for stratigraphy and ages caption). Note that fault B2
832 offsets vertically unconformity Ua (blue) and that sequence UTR2 sealed the Cabuyal fault
833 which offsets unit L3b; (d) Chirp data shows fault B2 and associated deformed strata; (d) map
834 showing line location.

835
836 **Figure 11.** Seismic reflection line SCAN-417 across the North (NCa) and South (SCa) Canoa
837 Faults; (a) un-interpreted section with crossing seismic lines; (b) interpreted section (see
838 Figure 2 and 4 for stratigraphy caption). Note the strong reflector (dark green) returned by the
839 eroded top of the basement high also identified in crossing line SCAN 900 (Fig. 2). This
840 segment of NCa fault is blind and sealed, whereas that of SCa fault might still accommodate
841 deformation; (c) map showing line location.

842
843 **Figure 12.** Structural map showing focal mechanisms of the 2016 aftershock sequence and
844 other geological and geophysical information within a N-83°E trending corridor bounded by
845 the two parallel dashed lines. The corridor includes (1) the shallowest Ecuadorian trench
846 segment (orange segment of the deformation front), (2) a morphologic scar in the outer
847 wedge, (3) the shallow shelf promontory and its broad composite green and yellow anticline
848 structures (see geology caption in Fig. 3), (4) the Cabo-Pasado and Jama locked asperities (CP
849 and J dark orange -yellow pattern, see Fig. 1c); (5) the 30-days after slip of the Mw 7.8, 2016
850 earthquake (thin black contours every 10 cm after Rolandone et al., 2018); (6) repeating
851 earthquakes (red stars) identified over a ~1 year period after the 2016 earthquake (Chalumeau
852 et al., 2021); and (7) the highest (51.4 cm) 2016-co-seismic uplift (vertical black arrow)
853 (Nocquet et al., 2017). The alignment of the northern cluster of repeaters departs from the
854 fault trends and may outlines structures of the north flank of the subducting CR crest, while
855 the near-trench cluster concentrates beneath the outer wedge scar left in the wake of the
856 subducting CR crest. Orange beach balls are thrust focal mechanisms from gCMT catalog

857 (<https://www.globalcmt.org>); blue ones are from Leon Rios et al., (2019). Note that four 2016
858 strike-slip focal mechanisms are associated with the Canoa fault system (NCa).

859
860 **Figure 13.** Time-calibrated sketch of the subduction of two reliefs of the Carnegie Ridge
861 (CR) crest hypothesized to be related the Cabo Pasado (CP) and Jama (J) inter-plate locked
862 asperities. The sketch accounts for the timing of major unconformities Ua (0.79 Ma), Ub (1.0
863 Ma) and Uc (1.8 Ma) and the successive main stages of margin wedge uplift and subsidence
864 (see Fig. 3 for tectonic pattern; dashed blue line is the present shelf edge). (i) Prior to ~1.8
865 Ma, an outer-wedge inter-plate coupling (pale orange trench-parallel strip) is necessary to
866 produce outer-wedge strain partitioning (black dashed arrow) and activate the BJ strike-slip
867 faulting (BJF). (ii) Between 1.8 and 1.0 Ma, the subduction of the CR crest reliefs increases
868 locally the inter-plate coupling (dark orange ellipses), blocking progressively the BJ fault
869 system, and uplifting the shelf promontory area. (iii) Between 0.8 and 0.6 Ma, the subduction
870 of an inferred topographic saddle between the “J” and “CP” reliefs leads to a local subsidence,
871 followed by the uplift of the shelf promontory due to the CP relief subduction. Uplift of
872 marine inner-shelf to continental deposits near the city of Jama occurred from ~1 Ma
873 (Cantalamessa et al., 2005). (iv) 0 Ma, although weaker than at the present-day CP and J
874 locked asperities, an outer-wedge inter-plate coupling may still operate. Vertical blue arrows
875 are 2016-co-seismic uplift in cm (Nocquet et al., 2017).

876

877

878 **References:**

879

880 Adam, J., Klaeschen, D., Kukowski, N., and Flueh, E. R. (2004), Upward delamination of
881 Cascadia Basin sediment infill with landward frontal accretion thrusting caused by rapid
882 glacial age material flux, *Tectonics*, 23(TC3009), doi:10.1029/2002TC001475,

883 Agurto-Detzel, H., Font, Y., Charvis, P., Régnier, M., Rietbrock, A., Ambrois, D., et al.

884 (2019), Ridge subduction and afterslip control aftershock distribution of the 2016 Mw 7.8

885 Ecuador earthquake, *Earth and Planetary Science Letters*, 530, 63-76,

886 10.1016/j.epsl.2019.05.029.

887 Allmendinger, R. W., Smalley, J. R., Bevis, M., Caprio, H., and Brooks, B. (2005), Bending

888 the Bolivian orocline in real time, *Geology*, 33, 905-908, 10.1130/G21779.1.

889 Baker, A., Allmendinger, R. W., Owen, L. A., and Rech, J. A. (2013), Permanent deformation
890 caused by subduction earthquakes in northern Chile, *Nature Geoscience*, 6,

891 10.1038/NGEO1789.

892 Baldock, J. W. (1983), The Northern Andes: A Review of the Ecuadorian Pacific Margin, in

893 *The Ocean Basins and Margins - The Pacific Ocean*, edited by A. E. Nairn, F. G. Stehli and

894 S. Uyeda, pp. 181-217, Plenum Press, New York and London.

- 895 Bassett, D., and Watts, A. B. (2015), Gravity anomalies, crustal structure, and seismicity at
 896 subduction zones: 1. Seafloor roughness and subducting relief, *Geochem. Geophys. Geosyst.*,
 897 *16*, 1508–1540, doi: 10.1002/2014GC005684.
- 898 Beck, M. E. (1983), On the mechanism of tectonic transport in zones of oblique subduction,
 899 *Tectonophysics*, *93*, 1-11,
- 900 Beck, M. E., Rojas, C., and Cembranos, J. (1993), On the nature of buttressing in margin-
 901 parallel strike-slip fault systems, *Geology*, *21*, 755-758,
- 902 Beck, S. L., and Ruff, L. J. (1984), The rupture process of the great 1979 Colombia
 903 earthquake: evidence for the asperity model, *Journal of Geophysical Research*, *89*, 9281-
 904 9291,
- 905 Béjar-Pizarro, M., Socquet, A., Armijo, R., Carrizo, D., Genrich, J., and Simons, M. (2013),
 906 Andean structural control on interseismic coupling in the North Chile subduction zone,
 907 *Nature Geoscience*, 10.1038/NGEO1802.
- 908 Bell, R., Holden, C., Power, W., Wang, X., and Downes, G. (2014), Hikurangi margin
 909 tsunami earthquake generated by slow seismic rupture over a subducted seamount, *Earth and*
 910 *Planetary Science Letters*, *397*, 1-9, doi: 10.1016/j.epsl.2014.04.005.
- 911 Berglar, K., Gaedicke, C., Lutz, R., Franke, D., and Djajadihardja, Y. S. (2008), Neogene
 912 subsidence and stratigraphy of the Simeulue forearc basin, Northwest Sumatra, *Marine*
 913 *Geology*, *253*, 1-13, 10.1016/j.margeo.2008.04.006.
- 914 Bilek, S. L., and Lay, T. (2018), Subduction zone megathrust earthquakes, *Geosphere*, *14*(4),
 915 p. 1468–1500, doi.org/10.1130/GES01608.1.
- 916 Cantalamessa, G., Di Celma, C., and Ragaini, L. (2005), Sequence stratigraphy of the Punta
 917 Ballena Member of the Jama Formation (Early Pleistocene, Ecuador): insights from integrated
 918 sedimentologic, taphonomic and paleoecologic analysis of molluscan shell concentrations,
 919 *Palaeogeography, Palaeoclimatology, Palaeoecology*, *216*, 1-25,
 920 10.1016/j.palaeo.2004.09.012.
- 921 Chalumeau, C., Agurto-Detzel, H., De Barros, L., Charvis, P., Galve, A., Rietbrock, A., et al.
 922 (2021), Repeating Earthquakes at the Edge of the Afterslip of the 2016 Ecuadorian MW 7.8
 923 Pedernales Earthquake, *Journal of Geophysical Research, Solid Earth*, *126*,
 924 e2021JB021746, 10.1029/2021JB021746.
- 925 Chemenda, A., Lallemand, S., and Bokun, A. (2000), Strain partitioning and interplate
 926 friction in oblique subduction zones: Constraints provided by physical modeling, *Journal of*
 927 *Geophysical Research*, *105*(3), 5567-5582,
- 928 Chlieh, M., Mothes, P. A., Nocquet, J.-M., Jarrin, P., Charvis, P., Cisneros, D., et al. (2014),
 929 Distribution of discrete seismic asperities and aseismic slip along the Ecuadorian Megathrust,
 930 *Earth and Planetary Science Letters*, *400*, 292-301, doi.org/10.1016/j.epsl.2014.05.027.
- 931 Collot, J.-Y., Marcaillou, B., Sage, F., Michaud, F., Agudelo, W., Charvis, P., et al. (2004),
 932 Are rupture zone limits of great subduction earthquakes controlled by upper plate structures ?
 933 : evidence from multichannel seismic reflection data acquired across the northern Ecuador -
 934 southwest Colombia margin, *Journal of Geophysical Research*, *109*, 1-14,
 935 10.1029/2004JB003060.
- 936 Collot, J.-Y., Migeon, S., Spence, G., Legonidec, Y., Marcaillou, B., Schneider, J.-L., et al.
 937 (2005), Seafloor margin map helps in understanding subduction earthquakes, *EOS*
 938 *Transactions, American Geophysical Union*, *86*(46), 464-466,
- 939 Collot, J. Y., Sanclemente, E., Nocquet, J. M., Leprêtre, A., Ribodetti, A., Jarrin, P., et al.
 940 (2017), Subducted oceanic relief locks the shallow megathrust in central Ecuador, *Journal of*
 941 *Geophysical Research, Solid Earth*, *122*, 10.1002/2016JB013849.
- 942 Davis, D. M., Suppe, J., and Dahlen, F. A. (1983), Mechanics of fold-and-thrust belts and
 943 accretionary wedges, *Journal of Geophysical Research*, *88*(B2), 1153-1172,

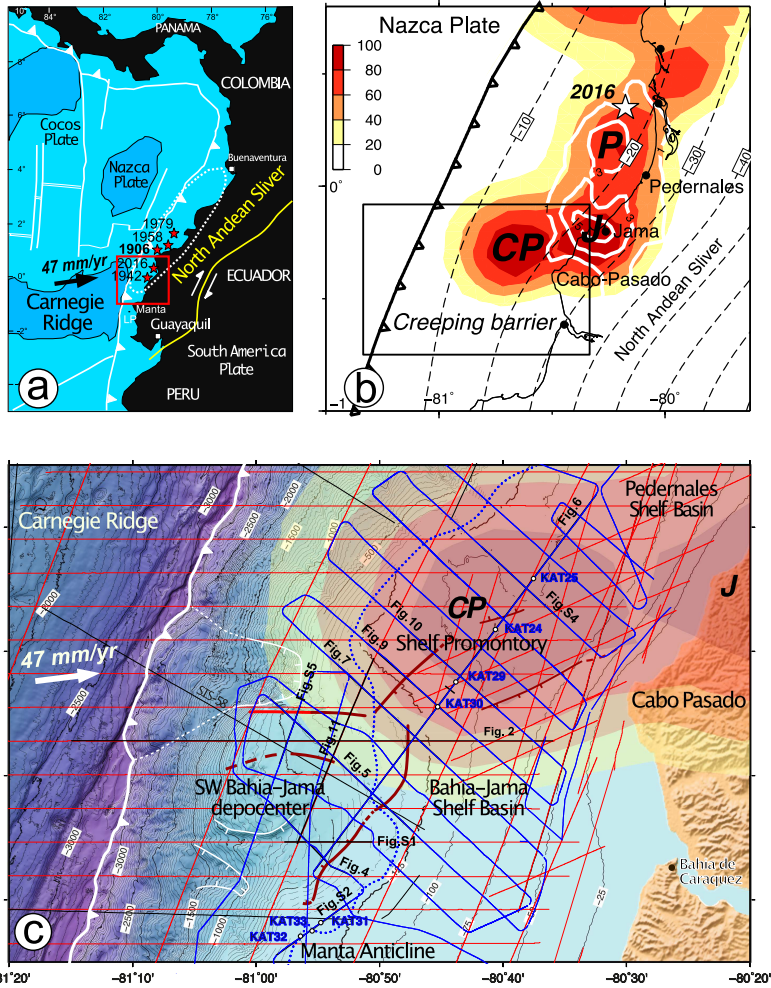
- 944 Diament, M., Harjono, H., Karta, K., Deplus, C., Dahrin, D., Zen, M. T. J., et al. (1992),
 945 Mentawai fault zone off Sumatra: A new key to the geodynamics of western Indonesia,
 946 *Geology*, *20*, 259-262,
- 947 Dominguez, S., Malavieille, J., and Lallemand, S. (2000), Deformation of margins in
 948 response to seamount subduction insights from sandbox experiments, *Tectonics*, *19*(1), 182-
 949 196,
- 950 Embry, A. F. (1993), Transgressive-regressive (T–R) sequence analysis of the Jurassic
 951 succession of the Sverdrup Basin, Canadian Arctic Archipelago, *Canadian Journal of Earth
 952 Sciences*, *30*, 301–320,
- 953 Fitch, T. J. (1972), Plate convergence, transcurrent faults, and internal deformation adjacent to
 954 Southeast Asia and the western Pacific, *Journal of Geophysical Research*, *77*, 4432-4460,
- 955 Font, Y., Segovia, M., Vaca, S., and Theunissen, T. (2013), Seismicity patterns along the
 956 Ecuadorian subduction zone: new constraints from earthquake location in a 3-D a priori
 957 velocity model, *Geophysical Journal International*, *193*, 263–286, doi: 10.1093/gji/ggs083.
- 958 Gagnon, K., C. D. Chadwell, E. Norabuena (2005), Measuring the onset of locking in the
 959 Peru–Chile trench with GPS and acoustic measurements, *Nature*, *434*, 205-207,
 960 doi:10.1038/nature03412.
- 961 Goldfinger, C., Nelson, C. H., Morey, A. E., Johnson, J. E., Patton, J. R., Karabanov, E., et al.
 962 (2012), Turbidite Event History—Methods and Implications for Holocene Paleoseismicity of
 963 the Cascadia Subduction Zone, *U. S. Geological Survey, Professional Paper 1661–F*,
 964 *Professional Paper 1661–F*, 170, <http://pubs.usgs.gov/pp/pp1661/f>
- 965 Gombert, B., Duputel, Z., Jolivet, R., Simons, M., Jiang, J., Liang, C., et al. (2018), Strain
 966 budget of the Ecuador–Colombia subduction zone: A stochastic view, *Earth and Planetary
 967 Science Letters*, *498*, 288-299, 10.1016/j.epsl.2018.06.046.
- 968 Graindorge, D., Calahorrano, A., Charvis, P., Collot, J.-Y., and Bethoux, N. (2004), Deep
 969 structures of the Ecuador convergent margin and the Carnegie Ridge, possible consequence
 970 on great earthquakes recurrence interval, *Geophysical Research Letters*, *31*(4, L04603),
 971 doi :10.1029/2003GL018803.
- 972 Gutscher, M. A., Malavieille, J., Lallemand, S., and Collot, J. Y. (1999), Tectonic
 973 segmentation of the North Andean margin: impact of the Carnegie Ridge collision, *Earth and
 974 Planetary Science Letters*, *168*, 255-270,
- 975 Hansen, J., Sato, M., Russell, G., and Kharecha, P. (2013), Climate sensitivity, sea level and
 976 atmospheric carbon dioxide, *Philosophical Transactions of the Royal Society of London, A
 977 371: 20120294*, 10.1098/rsta.2012.0294.
- 978 Hernández, M. J., Michaud, F., Collot, J.-Y., Proust, J.-N., and d'Acremont, E. (2020),
 979 Evolution of the Ecuador offshore nonaccretionary-type forearc basin and margin
 980 segmentation, *Tectonophysics*, *781*, 228374, 10.1016/j.tecto.2020.228374.
- 981 Jaillard, E., Lapierre, H., Ordoñez, M., Toro Álava, J., Amórtegui, A., and Vanmelle, J.
 982 (2009), Accreted oceanic terranes in Ecuador: southern edge of the Caribbean Plate?, in
 983 *Geological Society, London, Special Publications* edited, pp. 489-485.
- 984 Jara-Muñoz, J., Melnick, D., Zambrano, P., Rietbrock, A., González, J., Argandoña, B., and
 985 Strecker, M. R. (2017), Quantifying offshore forearc deformation and splay-fault slip using
 986 drowned Pleistocene shorelines, Arauco Bay, Chile, *Journal of Geophysical Research, Solid
 987 Earth*, *122*, 4529-4558, 10.1002/2016JB013339.
- 988 Jarrard, R. D. (1986a), Terrane motion by strike slip faulting of forearc slivers, *Geology*, *14*,
 989 780-783,
- 990 Jarrard, R. D. (1986b), Relations among subduction parameters, *Reviews of Geophysics*,
 991 *24*(2), 217-284,

- 992 Jolivet, R., Simons, M., Duputel, Z., Olive, J.-A., Bhat, H. S., and Bletery, Q. (2020),
 993 Interseismic Loading of Subduction Megathrust Drives Long-Term Uplift in Northern Chile,
 994 *Geophysical Research Letter*, *47*, e2019GL085377, 10.1029/2019GL085377.
- 995 Kame, N., Rice, J. R., and Dmowska, R. (2003), Effects of prestress state and rupture velocity
 996 on dynamic fault branching, *Journal of Geophysical Research*, *108*(B5, 2265),
 997 10.1029/2002JB002189.
- 998 Kanamori, H., and McNally, K. C. (1982), Variable rupture mode of the subduction zone
 999 along the Ecuador-Colombia coast, *Bulletin of the Seismological Society of America*, *72*(4),
 1000 1241-1253,
- 1001 Kelleher, J. (1972), Rupture zones of large South American earthquakes and some
 1002 predictions, *Journal of Geophysical Research*, *77*, 2087-2103,
 1003 doi:10.1029/JB077i011p02087.
- 1004 Koch, C. D., Lynner, C., Delph, J., Beck, S. L., Meltzer, A., Font, Y., et al. (2020), Structure
 1005 of the Ecuadorian forearc from the joint inversion of receiver functions and ambient noise
 1006 surface waves, *Geophysical Journal International*, *222*, 1671–1685, doi:
 1007 10.1093/gji/ggaa237.
- 1008 Lallemand, S., Liu, C.-S., Dominguez, S., Schnurle, P., Malavieille, J., and the ACT
 1009 Scientific Crew (1999), Trench-parallel stretching and folding of forearc basins and lateral
 1010 migration of the accretionary wedge in the southern Ryukyus: A case of strain partition
 1011 caused by oblique convergence, *Tectonics*, *18*(2), 231-247,
- 1012 Lallemand, S., Peyret, M., van Rijsingen, E., Arcay, D., and Heuret, A. (2018), Roughness
 1013 Characteristics of Oceanic Seafloor Prior to Subduction in Relation to the Seismogenic
 1014 Potential of Subduction Zones, *Geochem. Geophys. Geosyst.*, *19*, 2121–2146,
 1015 10.1029/2018GC007434.
- 1016 Lallemand, S. E., Schnurle, P. S., and Malavieille, J. (1994), Coulomb theory applied to
 1017 accretionary and non accretionary wedges: Possible causes for tectonic erosion and/or frontal
 1018 accretion, *Journal of Geophysical Research*, *99*, 12,033-012,055,
- 1019 León-Ríos, S., Agurto-Detzel, H., Rietbrock, A., Alvarado, A., Beck, S., Charvis, P., et al.
 1020 (2019), 1D-velocity structure and seismotectonics of the Ecuadorian margin inferred T from
 1021 the 2016 Mw7.8 Pedernales aftershock sequence, *Tectonophysics*, *767*,
 1022 10.1016/j.tecto.2019.228165.
- 1023 León-Ríos, S., Bie, L., Agurto-Detzel, H., Galve, A., Alvarado, A., Beck, S., et al. (2021), 3D
 1024 Local Earthquake Tomography of the Ecuadorian Margin in the Source Area of the 2016 Mw
 1025 7.8 Pedernales Earthquake, *Journal of Geophysical Research, Solid Earth*,
 1026 10.1029/2020JB020701.
- 1027 Liberty, L. M., Brothers, D. S., and Haeussler, P. J. (2019), Tsunamigenic Splay Faults Imply
 1028 a Long-Term Asperity in Southern Prince William Sound, Alaska, *Geophysical Research*
 1029 *Letter*, 10.1029/2018GL081528.
- 1030 Lieser, K., Grevemeyer, I., Lange, D., Flueh, E., Tilmann, F., and Contreras-Reyes, E. (2014),
 1031 Splay fault activity revealed by aftershocks of the 2010 Mw 8.8 Maule earthquake, central
 1032 Chile, *Geology*, 10.1130/G35848.1.
- 1033 Lisiecki, L. E., and Raymo, M. E. (2005), A Pliocene-Pleistocene stack of 57 globally
 1034 distributed benthic $\delta^{18}O$ records, *Paleoceanography*, *20*, doi:10.1029/2004PA001071,
- 1035 Lonsdale, P. (1978), Ecuadorian subduction system, *The American Association of Petroleum*
 1036 *Geologists Bulletin*, *62*(12), 2454-2477,
- 1037 Loveless, J. P., and Meade, B. J. (2011), Spatial correlation of interseismic coupling and
 1038 coseismic rupture extent of the 2011 MW = 9.0 Tohoku-oki earthquake, *Geophysical*
 1039 *Research Letters*, *38* (L17306), doi:10.1029/2011GL048561.
- 1040 Luzieux, L. D. A., Heller, F., Spikings, R., Vallejo, C. F., and Winkler, W. (2006), Origin and
 1041 Cretaceous tectonic history of the coastal Ecuadorian forearc between 1°N and 3°S:

- 1042 Paleomagnetic, radiometric and fossil evidence, *Earth and Planetary Science Letters*, 249,
 1043 400–414,
- 1044 Lynner, C., Koch, C., Beck, S. L., Meltzer, A., Soto-Cordero, M., Hoskins, M. C., et al.
 1045 (2020), Upper-plate structure in Ecuador coincident with the subduction of the Carnegie
 1046 Ridge and the southern extent of large mega-thrust earthquakes, *Geophysical Journal
 1047 International*, 220, 1965-1977, doi: 10.1093/gji/ggz558.
- 1048 Mann, P. (2007), Global catalogue, classification and tectonic origins of restraining- and
 1049 releasing bends on active and ancient strike-slip fault systems, in *Tectonics of Strike-Slip
 1050 Restraining and Releasing Bends*, edited by W. D. Cunningham and P. Mann, pp. 13-142,
 1051 Geological Society, London, Special Publications, London.
- 1052 Matsuura, M., and Sato, T. (1989), A dislocation model for the earthquake cycle at
 1053 convergent plate boundaries, *Geophysical Journal*, 96, 23-32,
- 1054 McCaffrey, R. (1992), Oblique plate convergence, slip vectors, and forearc deformation.,
 1055 *Journal of Geophysical Research*, 97, 8,905-908,915,
- 1056 McCaffrey, R., Zwick, P. C., Bok, Y., Prawirodirdjo, L., Genrich, J. F., Stevens, C. W., et al.
 1057 (2000), Strain partitioning during oblique plate convergence in northern Sumatra: Geodetic
 1058 and seismologic constraints and numerical modeling, *Journal of Geophysical Research*, 105,
 1059 B12, 23363-28376,
- 1060 Melgar, D., Fan, W., Riquelme, S., Geng, J., Liang, C., Fuentes, M., et al. (2016), Slip
 1061 segmentation and slow rupture to the trench during the 2015, Mw8.3 Illapel, Chile
 1062 earthquake, *Geophysical Research Letter*, 43, 10.1002/ 2015GL067369.
- 1063 Melnick, D. (2016), Rise of the central Andean coast by earthquakes straddling the Moho,
 1064 *Nature Geoscience*, 9, 10.1038/NGEO2683.
- 1065 Mendoza, C., and Dewey, J. W. (1984), Seismicity associated with the great Colombia-
 1066 Ecuador earthquakes of 1942, 1958 and 1979: implications for barrier models of earthquake
 1067 rupture, *Bulletin of the Seismological Society of America*, 74(2), 577-593,
- 1068 Michaud, F., Proust, J. N., Collot, J. Y., Lebrun, J. F., Witt, C., Ratzov, G., et al. (2015),
 1069 Quaternary sedimentation and active faulting along the Ecuadorian shelf: preliminary results
 1070 of the ATACAMES Cruise (2012), *Marine Geophysical Researches*, 36, 91-98,
 1071 10.1007/s11001-014-9231-y.
- 1072 Miller, K., G., Kominz, M. A., Browning, J. V., Wright, J. D., Mountain, G. S., Katz, G. S., et
 1073 al. (2005), The Phanerozoic Record of Global Sea-Level Change, *Science*, 310(1293), DOI:
 1074 10.1126/science.1116412.
- 1075 Moreno, M., Rosenau, M., and Oncken, O. (2010), 2010 Maule earthquake slip correlates
 1076 with pre-seismic locking of Andean subduction zone, *Nature Letters*, 46, 198-202,
 1077 10.1038/nature09349.
- 1078 Nocquet, J.-M., Villegas-Lanza, J. C., Chlieh, M., Mothes, P. A., Rolandone, F., Jarrin, P., et
 1079 al. (2014), Motion of continental slivers and creeping subduction in the northern Andes,
 1080 *Nature Geoscience*, 1-5, doi: 10.1038/NGEO2099.
- 1081 Nocquet, J.-M., Jarrin, P., Vallée, M., Mothes, P. A., Grandin, R., Rolandone, F., et al.
 1082 (2017), Supercycle at the Ecuadorian subduction zone revealed after the 2016 Pedernales
 1083 earthquake, *Nature Geoscience*, 10, 146-149, doi:10.1038/NGEO2864.
- 1084 Pennington, W. D. (1981), Subduction of the Eastern Panama Basin and seismotectonics of
 1085 northwestern South America, *Journal of Geophysical Research*, 86(B11), 10753-10770,
- 1086 Perfettini, H., Avouac, J.-P., Tavera, H., Kositsky, A., Nocquet, J.-M., Bondoux, F., et al.
 1087 (2010), Seismic and aseismic slip on the Central Peru megathrust, *Nature*, 465, 78-81, doi:
 1088 10.1038/nature09062.
- 1089 Philiposian, B., Sieh, K., Avouac, J.-P., Natawidjaja, D. H., Chiang, H. W., Wu, C.-C., et al.
 1090 (2014), Rupture and variable coupling behavior of the Mentawai segment of the Sunda

- 1091 megathrust during the supercycle culmination of 1797 to 1833, *Journal of Geophysical*
 1092 *Research*, 119, 7258-7287, 10.1002/2014JB011200.
- 1093 Popescu, S.-M. (2021), Plio-Pleistocene Foraminifera from Ecuador - biostratigraphy, 1-19
 1094 pp, GeobiostratData Consulting. <https://hal.archives-ouvertes.fr/hal-03669503>.
- 1095 Proust, J.-N., Martillo, C., Michaud, F., Collot, J.-Y., and Dauteuil, O. (2016), Subduction of
 1096 seafloor asperities revealed by a detailed stratigraphic analysis of the active margin shelf
 1097 sediments of Central Ecuador, *Marine Geology*, 380, 345-362, doi:
 1098 10.1016/j.margeo.2016.03.014.
- 1099 Proust, J. N., and Chanier, F. (2004), The Pleistocene cape Kidnappers section in New
 1100 Zealand: orbitally-forced controls on active margin sedimentation. , *Journal of Quaternary*
 1101 *Science*, 19(6), 591-603,
- 1102 Reyes, P., and Michaud, F. (2012), Mapa Geologico de la Margen Costera Ecuatoriana
 1103 (1/1500000), EPPetroEcuador-IRD Quito, Ecuador.
- 1104 Rolandone, F., Nocquet, J.-M., Mothes, P. A., Jarrin, P., Vallée, M., Cubas, N., et al. (2018),
 1105 Areas prone to slow slip events impede earthquake rupture propagation and promote afterslip,
 1106 *Science Advances*, 4:eaa06596,
- 1107 Ruh, J. B., Gerya, T., and Burg, J.-P. (2013), High-resolution 3D numerical modeling of
 1108 thrust wedges: Influence of décollement strength on transfer zones, *Geochem. Geophys.*
 1109 *Geosyst.*, 14(4), 1131-1155, 10.1002/ggge.20085.
- 1110 Ruh, J. B., Sallarès, V., Ranero, C. R., and Gerya, T. (2016), Crustal deformation dynamics
 1111 and stress evolution during seamount subduction: High-resolution 3-D numerical modeling,
 1112 *Journal of Geophysical Research, Solid Earth*, 121, doi: 10.1002/2016JB013250.
- 1113 Sage, F., Collot, J.-Y., and Ranero, C. R. (2006), Interplate patchiness and subduction-erosion
 1114 mechanisms : Evidence from Depth Migrated Seismic Images at the Central Ecuador
 1115 convergent margin, *Geology*, 34(12), 997-1000, doi: 10.1130/G22790A.1.
- 1116 Saillard, M., Audin, L., Rousset, B., Avouac, J.-P., Chlieh, M., Hall, S. R., and Farber, D. L.
 1117 (2017), From the seismic cycle to long-term deformation: linking seismic coupling and
 1118 Quaternary coastal geomorphology along the Andean megathrust, *Tectonics*, 241-256,
 1119 10.1002/2016TC004156.
- 1120 Sallares, V., Charvis, P., Flueh, E. R., Bialas, J., and scientific party Salieri (2005), Seismic
 1121 structure of the Carnegie Ridge and the nature of the Galàpagos Hotspot, *Geophysical Journal*
 1122 *International*, 161, 763-788,
- 1123 Sallares, V., and Ranero, C. (2019), Upper-plate rigidity determines depth- varying rupture
 1124 behaviour of megathrust earthquakes, *Nature*, 576, 96-101, org/10.1038/s41586-019-1784-0.
- 1125 Scholz, C. H. (1998), Earthquakes and friction laws, *Nature*, 391(1), 37-42,
- 1126 Schwartz, S. Y., and Rokosky, J. M. (2007), Slow slip events and seismic tremor at circum-
 1127 pacific subduction zones, *Reviews of Geophysics*, 45(RG3004),
- 1128 Somoza, R., and Ghidella, M. E. (2012), Late Cretaceous to recent plate motions in western
 1129 South America revisited, *Earth and Planetary Science Letters*, 331-332, 152-163,
 1130 10.1016/j.epsl.2012.03.003.
- 1131 Soto-Cordero, L., Meltzer, A., Bergman, E., Hoskins, M., Stachnik, J. C., Agurto-Detzel, H.,
 1132 et al. (2020), Structural control on megathrust rupture and slip behavior: Insights from the
 1133 2016 Mw 7.8 Pedernales Ecuador earthquake, *Journal of Geophysical Research: Solid Earth*,
 1134 125, e2019JB018001, <https://doi.org/10.1029/2019JB018001>.
- 1135 Swenson, J. L., and Beck, S. L. (1996), Historical 1942 Ecuador and 1942 Peru subduction
 1136 earthquakes, and earthquake cycles along Colombia-Ecuador and Peru subduction segments,
 1137 *Pageoph.*, 146(1), 67-101,
- 1138 ten Brink, U., and Lin, J. (2004), Stress interaction between subduction earthquakes and
 1139 forearc strike-slip faults: Modeling and application to the northern Caribbean plate boundary,
 1140 *Journal of Geophysical Research*, 109, B12310, 10.1029/2004JB003031.

- 1141 Tsuji, T., Kawamura, K., Kanamatsu, T., Kasaya, T., Fujikura, K., Ito, Y., et al. (2013),
 1142 Extension of continental crust by anelastic deformation during the 2011 Tohoku-oki
 1143 earthquake: The role of extensional faulting in the generation of a great tsunami, *Earth and*
 1144 *Planetary Science Letters*, *364*, 44-58, 10.1016/j.epsl.2012.12.038.
- 1145 Vaca, S., Vallée, M., Nocquet, J.-M., and Alvarado, A. (2019), Active deformation in
 1146 Ecuador enlightened by a new waveform-based T catalog of earthquake focal mechanisms,
 1147 *Journal of South American Earth Sciences*, *93*, 449-461, 10.1016/j.jsames.2019.05.017.
- 1148 Vail, P. R., Mitchum Jr., R. M., and Thompson III, S. (1977), Seismic stratigraphy and global
 1149 changes of sea level, part 3: relative changes of sea level from coastal onlap, in *American*
 1150 *Association of Petroleum Geologists* edited by C. E. Payton, pp. 63-81.
- 1151 van Dinther, Y., Gerya, T. V., Dalguer, L. A., Mai, P. M., Morra, G., and Giardini, D. (2013),
 1152 The seismic cycle at subduction thrusts: Insights from seismo-thermo-mechanical models,
 1153 *Journal of Geophysical Research, Solid Earth*, *118*, 6183-6202, 10.1002/2013JB010380.
- 1154 van Rijnsingen, E., Lallemand, S., Peyret, M., Arcay, D., Heuret, A., Funicello, F., and Corbi,
 1155 F. (2018), How subduction interface roughness influences the occurrence of large interplate
 1156 earthquakes., *Geochem. Geophys. Geosyst.*, *19*, 1-29, 10.1029/2018GC007618.
- 1157 Victor, P., Sobiesiak, M., Glodny, J., Nielsen, S. N., and Oncken, O. (2011), Long-term
 1158 persistence of subduction earthquake segment boundaries: Evidence from Mejillones
 1159 Peninsula, northern Chile, *Journal of Geophysical Research*, *116*(B02402),
 1160 10.1029/2010JB007771.
- 1161 von Huene, R., and Scholl, D. W. (1991), Observations at convergent margins concerning
 1162 sediment subduction, subduction erosion, and growth of continental crust, *Reviews of*
 1163 *Geophysics*, *29*, 279-316,
- 1164 Wallace, L. M., Webb, S. C., Ito, Y., Mochizuki, K., Hino, R., Henrys, S., et al. (2016), Slow
 1165 slip near the trench at the Hikurangi subduction zone, New Zealand, *Science*, *352*(6286), 701-
 1166 704, doi: 10.1126/science.aaf2349.
- 1167 Wang, K. (1996), Simplified Analysis of horizontal stresses in a buttressed forearc sliver at an
 1168 oblique subduction zone, *Geophysical Research Letter*, *23*(16), 2021-2024,
- 1169 Wang, K., and Dixon, T. (2004), "Coupling" Semantics and Science in Earthquake Research,
 1170 *EOS Transactions, American Geophysical Union*, *85*(18), 179-180,
- 1171 Wang, K., and Hu, Y. (2006), Accretionary prisms in subduction earthquake cycles : the
 1172 theory of dynamic Coulomb wedge, *Journal of Geophysical Research*, *111*(B06410),
 1173 10.1029/2005JB004094,
- 1174 Wang, K. (2010), Finding Fault in Fault Zones, *Science*, *329*(152), 10.1126/science.1192223.
- 1175 Wang, K., and Bilek, S. L. (2014), Invited review paper: Fault creep caused by subduction of
 1176 rough seafloor relief, *Tectonophysics*, *610*, 1-24, doi: 10.1016/j.tecto.2013.11.024.
- 1177 Wessel, P., and Smith, W. D. (1998), New, improved version of Generic Mapping Tools
 1178 Released, *EOS Transactions, American Geophysical Union*, *79*(47), 579,
- 1179 Yamaguchi, A., Sakaguchi, A., Sakamoto, T., Iijima, K., Kameda, J., Kimura, G., et al.
 1180 (2011), Progressive illitization in fault gouge caused by seismic slip propagation along a
 1181 megasplay fault in the Nankai Trough, *Geology*, *39*(11), 10.1130/G32038.1.
- 1182 Ye, A., Kanamori, H., Avouac, J.-P., Li, L., Fai Cheung, K., and Lay, T. (2016), The 16 April
 1183 2016, MW7.8(MS7.5) Ecuador earthquake: Aquasi-repeat of the 1942 MS7.5 earthquake and
 1184 partial re-rupture of the 1906 MS8.6 Colombia–Ecuador earthquake, *Earth and Planetary*
 1185 *Science Letters*, *454*, 248-258,
- 1186 Yilmaz, O. (2001), *Seismic Data Analysis. Processing, inversion and interpretation of*
 1187 *Seismic Data.* , 2065 pp., Society of Exploration Geophysicist.
- 1188 Yokota, Y., Ishikawa, T., Watanabe, S.-i., Tashiro, T., and Asada, A. (2016), Seafloor
 1189 geodetic constraints on interplate coupling of the Nankai Trough megathrust zone, *Nature*,
 1190 *534*, 10.1038/nature17632.



This article has been accepted for publication and undergone full peer review but has not been through the copyediting, typesetting, pagination and proofreading process, which may lead to differences between this version and the [Version of Record](#). Please cite this article as [doi: 10.1029/2022JB024192](https://doi.org/10.1029/2022JB024192).

This article is protected by copyright. All rights reserved.

